Subcellular imaging of lipids and sugars using genetically encoded proximity sensors

William M. Moore[1], Roberto J. Brea[1§], Caroline Knittel[1], Ellen Wrightsman[1], Brandon Hui[1], Jinchao Lou[2], Christelle F. Ancajas[2], Michael D. Best[2], Neal K. Devaraj[1], and Itay Budin[1*]

[1] Department of Chemistry and Biochemistry, University of California San Diego, 9500 Gilman Drive, La Jolla, California 92093

[2] Department of Chemistry, The University of Tennessee, Knoxville, Tennessee 37996

§ Current address: Centro Interdisciplinar de Química e Bioloxía (CICA), Universidade da Coruña, Rúa As Carballeiras, 15701 A Coruña, Spain

* To whom correspondence should be addressed: ibudin@ucsd.edu

Abstract

Live cell imaging of lipids and other metabolites is a long-standing challenge in cell biology. Bioorthogonal labeling tools allow for the conjugation of fluorophores to several phospholipid classes, but cannot discern their trafficking between adjacent organelles or asymmetry across individual membrane leaflets. Here we present fluorogen-activating coincidence sensing (FACES), a chemogenetic tool capable of quantitatively imaging subcellular lipid pools and reporting their transbilayer orientation in living cells. FACES combines bioorthogonal chemistry with genetically encoded fluorogen-activating proteins (FAPs) for reversible proximity sensing of conjugated molecules. We first validate this approach for quantifying discrete phosphatidylcholine pools in the ER and mitochondria that are trafficked by lipid transfer proteins. We then show that transmembrane domain-containing FAPs can be used to reveal the membrane asymmetry of multiple lipid classes that are generated in the trans-Golgi network. Lastly, we demonstrate that FACES is a generalizable tool for subcellular bioorthogonal imaging by measuring changes in mitochondrial *N*-acetylhexosamine levels. These results demonstrate the use of fluorogenic tags for spatially-defined molecular imaging.

Introduction

Lipid composition determines the biophysical properties of cell membranes and varies across every scale of biological organization: from tissues, to organelles, and even between individual leaflets of the same bilayer[1–3]. Investigating membrane chemical heterogeneity remains a challenge due to the paucity of tools for imaging lipids in live cells. Bioorthogonal 'click' chemistry has emerged as one tool for fluorescence labeling of specific lipid classes – including phosphatidylcholine (PC)[4], phosphatidylserine (PS)[5], phosphatidylinositol (PI)[6], phosphatidic acid[7], and glycosphingolipids[8] – that can be metabolically tagged with azide-bearing head group components (Fig. 1a). Azido (N_3) lipids are commonly conjugated to fluorophores using strain-promoted azide-alkyne cycloaddition (SPAAC) reactions, unveiling their cellular distribution once unreactive dyes are washed out. While powerful, this approach indiscriminately labels all lipids in the cell, and is thus limited by the resolution constraints of light microscopy: this approach cannot discriminate between lipid pools in organelles at close proximity or in individual leaflets of the same membrane, for example. To overcome some of these limitations, organelle-targeted fluorophores have been elegantly applied to image subcellular lipid pools[9]. Currently, these are limited to just a few chemical environments in the cell, such as rhodol-containing groups that localize to both endoplasmic reticulum (ER) and Golgi membranes, and thus lack additional specificity or resolution. They also depend on the self-segregation of dyes within the cell based on chemical cues, like membrane potential, which can be perturbed by lipid manipulation. We currently lack generalizable strategies to measure intracellular lipid heterogeneities in live cells and therefore cannot determine the molecular mechanisms by which they are generated.

We hypothesized that challenges for lipid imaging could be overcome using protein-based lipid sensors, whose localization is precisely controlled through signal sequences or fusion to other

60 protein components. Previously, natural lipid binding proteins derived from microbial toxins, such
61 as perfringolysin O[10] (cholesterol) or equinatoxin II[11] (sphingomyelin, SM) have been expressed
62 as fusions with fluorescent proteins (FP), to detect membranes enriched in the target lipids. In
63 these modalities, lipids are qualitatively detected by binding of the probe to a membrane, but
64 this limits their application to large compartments for which membrane binding is observable
65 and does not allow for quantitative detection. We asked whether 'turn on' fluorophores, termed
66 fluorogen-activating proteins (FAPs), could provide a more generalizable strategy. FAPs are
67 expressed as fusion constructs with other proteins or targeting sequences, similar to FPs, but
68 are not themselves fluorescent[12]. Instead, they interact with fluorogens, small cell-permeable
69 molecules that act as fluorophores only upon specific binding to a FAP (Fig. 1b). Depending on
70 the FAP used, fluorogen binding can be irreversible or reversible; the former provides brighter
71 fluorescence for conventional imaging, while the latter generates stochastic blinking that can be
72 harnessed for super-resolution imaging[13]. Recently, FAP domains have been applied towards
73 detecting and controlling protein proximity in living cells through reversible dimerization[14],
74 demonstrating that this technology can be harnessed in new applications beyond the capacity of
75 FPs.
76
77 We sought to harness the unique properties of fluorogens through Fluorogen-Activating
78 Coincidence Sensing (FACES), which uses the FAP protein for proximity-dependent reporting of
79 fluorogen conjugated bioorthogonal metabolites, including lipids. To accomplish this, we
80 synthesized fluorogenic dyes based on malachite green (MG) that are functionalized with a
81 dibenzocyclooctyne (DBCO) group for SPAAC reactions with azido-labeled metabolites in living
82 cells (Fig. 1c). In the FACES workflow (Fig. 1d), cells first express a FAP protein fused to an FP,
83 like GFP, that is targeted to an organelle or site of interest. Cells are then incubated with
84 azido-labeled metabolites for metabolic incorporation. Immediately before imaging, incorporated
85 metabolites are rapidly labeled with fluorogen-DBCO, which remains non-fluorescent unless it is

proximal to the expressed FAP. Excess dye is removed from cells by washing with culture medium, leveraging the reversibility of the FAP-fluorogen complex to prevent detection of unreacted fluorogens. Subsequent ratiometric fluorescence imaging allows organelle-specific detection of fluorogen conjugates by coincidence sensing with the FAP receptor. The abundance of the target molecule is then quantified at the locale of interest by measuring the ratio of FAP-fluorogen fluorescence, which represents the bound state of the FAP and is at red shifted wavelengths for MG, to that of a green of blue reporter FP, which is used to normalize the rate of detection to the concentration of the FAP receptor.

Here we validate the FACES strategy through imaging of discrete N_3-lipid pools in the ER, mitochondria, and trans-Golgi network (TGN). Ratiometric imaging with FACES enabled changes in N_3-lipid content of membranes to be quantified, which we use to characterize the role of ER-mitochondrial PC transporters. We then show that transmembrane-anchored FAPs can probe membrane asymmetry generated during vesicle formation at the TGN. Lastly, we demonstrate that FACES is a broadly applicable tool compatible with non-lipid metabolites by measuring fluctuations in mitochondrial *N*-acetylhexosamine (HexNAz) levels.

Results

Development and validation of FACES

We synthesized derivatives of MG with a linker and DBCO group, compatible with copper-free SPAAC reactions, including compound **1a** (Fig. 1c; Supplementary Fig. 1). MG non-covalently binds to single-chain antibody scFvs FAP and the complex emits far-red fluorescence. We tested the compatibility and fluorogenic properties of **1a** with FACES using the FAP clone dH6.2, a lower affinity scFvs variant developed for reversible equilibrium binding to MG[15]. In all

experiments, we fused dH6.2 – from here on simply referred to as FAP – to GFP for ratiometric imaging. A secretion signal and KDEL retention sequence were first used to target FAP-GFP to the endoplasmic reticulum (ER) as the major site of PC synthesis[16] (Fig 1c), while GFP-KDEL, an identical construct but lacking the FAP domain, was used as a control. HeLa cells transfected with either FAP-GFP-KDEL or GFP-KDEL were grown for 24h in the presence or absence of 50 μM N_3-Cho. At concentrations up to 100 μM, N_3-Cho was incorporated into PC at a frequency up to 0.1 mol %, but cells showed no detectable N_3-Cho incorporation into SM (Supplementary Fig. 2). Prior to staining, cells were washed and grown in normal growth media for 30 min to allow for the metabolic consumption of any remaining N_3-Cho. Cells were then transferred into FBS-free growth media containing 500 nM **1a** and imaged while in the staining solution (Fig. 2a). Images were collected using identical acquisition and processing settings.

Results from pre-washed cells demonstrated that **1a** was cell permeable and generated strong far-red fluorescence in cells expressing FAP-GFP-KDEL. No far-red fluorescence was detected in cells expressing GFP-KDEL, indicating that **1a** fluorescence was not activated directly by conjugation to N_3-PC. Next we tested the reversibility of the FAP-fluorogen complex by washing cells with growth medium and re-imaging (Fig. 2b). Three washes were sufficient to dissociate free **1a** from FAP-GFP-KDEL cells in the absence of N_3-Cho, resulting in the loss of far-red fluorescence. In contrast, far-red fluorescence was retained in FAP-GFP-KDEL cells that were fed 50 μM N_3-Cho, which implicated the SPAAC reaction product **1a**-PC as the source of FAP-dependent fluorescence. Similar experiments with a higher affinity FAP variant retained far-red fluorescence after washing in the absence of N_3-Cho labeling (Supplementary Fig. 3), indicating that the reversible binding to the MG product is essential for substrate-specific detection.

137 We further quantified these results in repeated experiments using confocal laser scanning
138 microscopy (CFLSM) to assess linear fluorescent detection. Cells transfected with
139 FAP-GFP-KDEL were fed 10, 30, or 50 μM N_3-Cho for 24h, while FAP-GFP-KDEL (no N_3-Cho)
140 and GFP-KDEL (+ 50 μM N_3-Cho) conditions were used as controls. All cells were stained with
141 500 nM **1a** and were washed as previously described; the **1a**-PC reaction product was
142 confirmed by LC/MS/MS (Supplementary Fig. 4). Fluorescence intensity profiles revealed that
143 far-red fluorescence from **1a** was tightly correlated with GFP fluorescence in FAP-GFP-KDEL
144 cells fed 50 μM N_3-Cho (Fig. 2c). In contrast, cells from either control condition, lacking the FAP
145 or N_3-Cho component, had low levels of far-red fluorescence that did not correlate with GFP
146 localization (Fig. 2c). The average fluorescence intensity from 10 cells, using 10 individual ER
147 segments per cell, was calculated as a ratiometric average relative to GFP. There was no
148 intensity difference between either control condition, while signal from FAP-GFP-KDEL cells fed
149 50 μM N_3-Cho was 10-fold higher (Fig. 2d). Additionally, **1a**-PC fluorescence was linearly
150 dependent on N_3-Cho concentration in the medium (Fig. 2e). We further tested whether the
151 FACES signal was a consequence of free N_3-Cho, as opposed to membrane incorporated
152 N_3-PC, by using compound D609 to pharmacologically perturb PC metabolism[17–19]. Cells treated
153 with 50 μM D609 during the 24h N_3-Cho incorporation period decreased FACES fluorescence
154 by 50% relative to untreated cells, despite being exposed to identical concentrations of N_3-Cho
155 and **1a** (Fig. 2f). Together, these results indicate that FACES is capable of linear fluorescent
156 quantification of N_3-PC, via its SPAAC reaction product **1a**-PC, in the ER of living cells.
157
158 <u>FACES quantifies lipid transport between organelle pools</u>
159
160 PC is the most abundant lipid in mammalian cells and is a component of all organelle
161 membranes, which make disentangling its subcellular transport mechanisms challenging. To
162 demonstrate the utility of the FACES method in illuminating organelle selective lipid pools, we

163 used the OTC mitochondrial targeting sequence (MTS) to direct FAP-GFP to the mitochondrial
164 matrix. Cells expressing MTS-FAP-GFP and the ER marker Sec61b-mCherry showed that
165 **1a**-PC in mitochondria did not overlap with the ER (Fig, 3a). Reciprocally, cells co-expressing
166 FAP-GFP-KDEL and MTS-BFP show that **1a**-PC in the ER did not overlap with mitochondria
167 (Fig. 3b).
168
169 When quantifying the performance of FACES in the mitochondrial matrix using CFLSM, we
170 found that switching the C6 alkane linker in **1a** to a polyethylene glycol (PEG)-2 linker
171 (compound **1b**) was beneficial for dissociating unreacted dye from this compartment. Similar to
172 the ER-targeted protein, MTS-FAP-GFP detection of **1b**-PC generated fluorescence that linearly
173 correlated with N_3-Cho concentration (Supplementary Fig. 5). Using super-resolution
174 lattice-structured illumination microscopy (lattice SIM[2]), we further tested whether the matrix
175 soluble FAP could resolve structural features of the IMM. When imaged by lattice SIM[2], FACES
176 signal from **1b**-PC occurred in a banding pattern distinct from the general distribution of the
177 probe (GFP signal) in the mitochondrial matrix (Fig. 3c). Fluorescence intensity profiles drawn
178 across individual mitochondria show undulating peaks, with alternating maxima between **1b**-PC
179 and GFP. We interpreted this localization pattern as reflecting regions of high cristae density in
180 the IMM that contrast with void areas of the matrix[20], as previously observed for mitochondrial
181 PC[9].
182
183 Utilizing the ability to quantify PC in mitochondria and ER, we tested how defects in lipid
184 transport differentially affect these pools. For this, we generated stable cell lines expressing
185 either FAP-GFP-KDEL (ER) or MTS-FAP-GFP (mitochondria) for further experiments. PC is
186 synthesized in the ER and is transported to mitochondria by lipid transport proteins (LTPs)[16,21].
187 We used siRNA to silence two LTPs: VPS13a, a bridge-type LTP that interacts with VAPB at
188 ER-mitochondria contact sites and transports bulk phospholipids[22], and StarD7, a small

189 shuttle-type LTP that localizes to the mitochondrial intermembrane space and is thought to
190 transport PC between outer and inner membranes[23–25] (Fig. 2d). Silencing resulted in a >50%
191 reduction in both VPS13a and StarD7 protein content in each experiment (Supplementary Fig.
192 6). VPS13a and StarD7 siRNAs reduced **1b**-PC fluorescence in mitochondria, by 50% and 35%
193 respectively, relative to negative control (NC) siRNA treated cells (Fig. 3e). However, only
194 knockdown of VPS13a increased **1a**-PC fluorescence in the ER (Fig. 3f), consistent with its
195 proposed role as an ER to mitochondrial PC LTP and that of StarD7 as an intra-mitochondrial
196 LTP. The magnitude of **1b**-PC reduction in mitochondria was larger upon knockdown of VPS13a
197 than for that of StarD7, suggesting that the former is a dominant mechanism for bulk PC
198 transport to mitochondria.
199
200 <u>FACES measures transbilayer asymmetry arising in the TGN</u>
201
202 It has long been recognized that membrane compartmentalization inherently generates
203 directionality between exoplasmic and cytoplasmic leaflets, which is reflected both in membrane
204 protein topology and the transbilayer distribution of lipids[26]. Detailed lipidomic investigation of
205 membrane asymmetry has only been carried out in the PM of erythrocytes, whose lack of
206 intracellular compartments allow for calculation of lipid accessibility to externally added
207 phospholipases[3,27]. While asymmetry is an emerging concept in membrane biology, the
208 transbilayer distribution of phospholipids in intracellular membranes is poorly understood. There
209 exists few, if any, tools capable of measuring membrane asymmetry in living cells and we asked
210 if the spatial specificity of FACES could provide this capacity.
211
212 A potential site of asymmetry generation in the secretory pathway is at the TGN, where vesicles
213 bud off from the Golgi for trafficking of proteins and lipids to the highly asymmetric PM. We
214 explored asymmetric lipid detection in the TGN by reciprocal tagging of the transmembrane

215 protein TGN38, at N- and C-termini, to selectively orient FAPs toward either the exoplasmic or
216 cytoplasmic facing leaflets of the TGN (Fig. 4a). TGN38 cycles to and from the PM via secretory
217 vesicles and recycling endosomes[28], thereby labeling a split population of trans-Golgi cisternae
218 and trans-Golgi network vesiculated compartments[29]. Imaging of stable cells expressing
219 GFP-TGN38-FAP, oriented towards the cytoplasmic leaflet, and FAP-TGN38-GFP, oriented
220 towards the luminal leaflet, detected fluorogen fluorescence of **1a**-PC on both leaflets in
221 cisternae and vesicles (Fig. 4b). However, the abundance shifted between these compartments,
222 comparatively enriching in the cytoplasmic leaflet in TGN vesicles. Lateral segregation between
223 luminal **1a**-PC enriched and depleted regions could be observed at sites of vesicular budding
224 from the TGN (Supplementary Fig. 7a). These results are consistent with previous
225 measurements of PC in freeze-fractured yeast cells, also showing a cytoplasmic leaflet
226 enrichment arising in the Golgi[30].
227
228 We next asked if FACES could measure the asymmetry of non-choline lipids at the TGN.
229 Recently, metabolic incorporation of azide containing L-serine[5] (C-L-Ser-N_3) and *myo*-inositol[6]
230 (Ino-N_3) have been shown to label phosphatidylserine (PS) and phosphatidylinositol (PI),
231 respectively. Both these lipid classes are synthesized in the ER and have been proposed to be
232 trafficked to the cytoplasmic leaflet of the trans-Golgi and TGN through lipid transfer proteins[31,32].
233 When analyzed with FACES, we observed **1a**-PI in Golgi cisternae that was evenly distributed
234 between luminal and cytoplasmic leaflets (Fig. 4c, Supplementary Fig. 8a). In TGN vesicles, the
235 distribution of **1a**-PI shifted to the cytoplasmic leaflet, similar to that for PC. For **1a**-PS, using
236 C-L-Ser-N_3, there was an absence of signal on both leaflets of Golgi cisternae and a high,
237 exclusively cytoplasmic abundance on TGN vesicles (Fig. 4c, Supplementary Fig. 8b). This is
238 consistent with previous observations that the PS-binding C2 domain of lactadherin, when
239 expressed in the cytoplasm, robustly labels TGN vesicles, but not Golgi cisternae[33]. As a control
240 for these cytosolic leaflet-enriched phospholipids, we imaged the distribution of surface glycans

241 in cells fed with peracetylated *N*-azidoacetylmannosamine (Ac_4ManNAz)[34], which is metabolized
242 into sialic acid (Sia) within the cell. We measured an exclusively luminal distribution of **1a**-Sia
243 (Fig. 4c, Supplementary Fig. 8c) in both cisternae and vesicles, consistent with the synthesis of
244 protein and lipid surface glycans in the Golgi lumen[35]. Lastly, co-staining cells expressing
245 mCer3-TGN38-FAP (Blue FP variant) with equimolar amounts **1a** and BODIPY-DBCO, a
246 conventional fluorophore, demonstrated that FACES can spectrally separate organelle-specific
247 lipid pools that overlap with total cellular phospholipid distributions (Supplementary Fig. 9)
248
249 Previous analyses of TGN vesicles[36] and the PM[37] suggest that loss of luminal phospholipids
250 could be substituted with SM, which is predominantly synthesized in the TGN and packaged in
251 secretory vesicles. Consistent with this model, we observed that the SM probe SMeqt-GFP
252 co-localized with vesicles enriched with cytoplasmic leaflet **1a**-PC (Fig. 4d). These vesicles
253 shuttled rapidly between the Golgi and PM (Supplementary Movie 1). Similar results were
254 obtained for vesicles labeled with the secretory cargo mCherry-GPI (Supplementary Fig. 10,
255 Supplementary Movie 2), which also co-traffics with SM in secretory vesicles[11]. Overall, these
256 results support a model in which phospholipids redistribute to the cytoplasmic leaflet during
257 TGN vesicularization (Fig 4d), while the luminal leaflet becomes enriched in newly synthesized
258 sphingolipids.
259
260 <u>FACES reports on changes to mitochondrial glycans</u>
261
262 Based on our detection of surface glycans in the Golgi lumen, we asked whether FACES could
263 be used as a general tool compatible for imaging of azido-sugars in living cells.
264 *N*-azidoacetylgalactosamine-tetraacylated (Ac_4GalNAz) is widely used as a metabolic reporter
265 for glycoconjugates containing *N*-acetylhexosamines (HexNAc)[38]. Ac_4GalNAz fed to cells is
266 converted to UDP-*N*-azidoacetylgalactosamine (UDP-GalNAz) by the hexosamine salvage

267 pathway and is then further epimerized to UDP-*N*-azidoacetylglucosamine (UDP-GlcNAz). This
268 results in robust labeling of *N*- and *O*- linked glycoproteins on the cell surface[38,39], secretory
269 compartments where they are formed, and endosomal compartments where they are recycled
270 (Fig 5a). Meanwhile, intracellular protein glycosylation is modulated by nucleocytoplasmic and
271 mitochondrial *O*-linked β-*N*-acetylglucosamines (*O*-GlcNAc), which are added to
272 serine/threonine residues by *O*-GlcNAc transferase (OGT) and removed by *O*-GlcNAcase
273 (OGA)[38]. *O*-GlcNAc cycling has emerged as a regulator of metabolism, signaling, and immune
274 evasion of cancer cells[40–42] and mitochondrial motility in neurons[43]. However, intracellular
275 glycosylations are not readily observed by standard bioorthogonal imaging approaches due to
276 the much more extensive incorporation of Ac_4GalNAz into surface glycans; very little signal from
277 conjugated conventional fluorophores co-localizes with mitochondria, for example (Fig. 5b).
278 Currently, detection of *O*-GlcNAcylation is performed in fixed cells or bulk extracts using
279 *O*-GlcNAc sensitive antibodies[44].
280
281 Using MTS-FAP-GFP expressing cells, we tested the efficacy of FACES in reporting
282 mitochondrial-specific changes in HexNAc. Cells were grown in the presence or absence of
283 either 100 μM Ac_4GalNAz or 100 μM *N*-azidoacetylglucosamine-tetraacylated (Ac_4GlcNAz) for
284 24h. Ac_4GlcNAz is not efficiently incorporated by the hexosamine salvage pathway[38] and thus
285 was used as a less metabolically active surrogate. SPAAC staining with **1b** generated
286 fluorescence signal intensities 10-fold greater in cells fed 100 μM Ac_4GalNAz compared to unfed
287 control cells (Fig. 5c). In contrast, **1b** fluorescence from cells fed Ac_4GlcNAz, which is less
288 efficiently incorporated into glycosylated proteins, was significantly lower than that for
289 Ac_4GalNAz, indicating that the FACES signal from **1b**-HexNAz is from sugars that have been
290 metabolically incorporated and not due to free azido sugars.
291

292 Next we tested whether FACES can report changes to mitochondrial *O*-GlcNAc levels resulting
293 from pharmacological treatment or nutritional state. We found that the OGA inhibitor Thiemet-G
294 increased **1b**-HexNAz fluorescence, suggesting that the fluorogen signal was responsive to the
295 activity of *O*-GlcNAc modifying enzymes (Fig 5d). In cancer cells, glucose uptake is positively
296 correlated with *O*-GlcNAc levels, which in-turn reprogram cellular metabolism tailored towards
297 glucose availability[45]. We observed that switching cells from high (30 mM) to low glucose (5.5
298 mM) levels during Ac_4GalNAz labeling reduced **1b**-HexNAz fluorescence by 30% (Fig. 5e). This
299 is similar to glucose-dependent changes in mitochondrial *O*-GlcNAc levels previously reported
300 in breast cancer cells[46]. Taken together, these data demonstrate that FACES can report
301 changes in mitochondrial HexNAz incorporation as a function of cell metabolism and
302 *O*-GlcNAcylation in living cells, and support the hypothesis that mitochondrial *O*-GlcNAcylation
303 is a post-translational modification that is responsive to the cell's dietary state.
304

305 **Discussion**

306

307 Studying cellular roles for non-proteinaceous biomolecules has long been hindered by the lack
308 of robust tools for their imaging in live cells. Here we introduce a new approach, FACES, that
309 combines the chemical specificity of metabolic incorporation with the spatial control of genetic
310 protein tagging for imaging of cellular metabolites. FACES harnesses reversible fluorogenic
311 systems, where fluorescence increases many orders of magnitude upon specific binding to a
312 FAP. It combines this turn on fluorescence with the specificity of bioorthogonal reactions for
313 molecular sensing. We highlight the use of this approach for subcellular imaging of
314 phospholipids, their transport between organelles, and orientations across membrane leaflets.
315 We propose that FACES is a generalizable tool that can be applied to other biomolecules.
316 Metabolic labeling has emerged as a particularly important tool for glycobiology and we

317 demonstrate that FACES is responsive to labeled glycoproteins in mitochondria, which have
318 been proposed to act as regulators of metabolic function[47].
319
320 Compared to other bioorthogonal imaging modalities, FACES has several key advantages for
321 mechanistic cell biology. For organelle-defined imaging, protein targeting sequences are more
322 specific and generalizable than corresponding chemically-encoded localization tags. We show
323 that this capacity can be applied to quantitative characterization of lipid distribution phenotypes
324 affected by trafficking networks across membrane contact sites. Beyond organelle-specific
325 imaging, FAPs can also be fused to specific proteins, allowing FACES-based detection of
326 molecules in defined nanoenvironments. Demonstrated is one such application, where FAP
327 domains are introduced on both sides of a TMD to read out bilayer asymmetry. Here, FACES
328 provides effective discrimination beyond what is possible with direct fluorescence imaging, as
329 the distance between two bilayer leaflets is less than 4 nm. Fluorogens show no fluorescence
330 when unbound to their corresponding FAP, so quantitative detection of conjugate products
331 occurs through the resulting fluorescence signal, not a change in its localization as for lipid
332 binding proteins. Because of this capacity, FACES is the only method, to our knowledge, that
333 allows for measurement of membrane asymmetry in live cells.
334
335 Applications of FACES could be further expanded through increases in the repertoire of
336 metabolic labeling, bioorthogonal chemistry, and the spectral plasticity of the fluorogen
337 employed. Conjugation of fluorogens to biomolecules is dependent on tagged metabolite
338 incorporation, which are continuously expanding across biological systems[48] and molecular
339 classes[49]. One concern with any metabolic labeling approach is that tagged molecules might not
340 fully mimic native compounds, which is especially relevant for lipids with minimal headgroups.
341 For several azido lipids, previous studies suggest that compounds localize across a range of
342 cells as expected[4,5], though it is challenging to preclude all differences between labeled and

343 unlabeled species. An additional limitation common to bioorthogonal approaches is the time
344 required for conjugation and washing out of unreacted fluorogens; these might make the
345 analysis of rapid redistributions of the underlying labeled species, like those relevant for lipid
346 signaling[50], challenging. Tuning fluorogenic reagents for faster conjugations[51] and washing could
347 decrease the time for processing steps to capture dynamic movements. Lastly, FACES could
348 also be broadened to utilize other fluorogen systems, including those based on the Photoactive
349 Yellow Protein[52] and bacterial lipocalin[53]. The MG-based system employed here was chosen
350 because of its very low background fluorescence in the unbound state. Because of the single
351 wavelength emission of the bound MG, measurements in two environments were taken across
352 multiple cells in separate experiments. Further development of multi-color FACES systems
353 would enable simultaneous detection of multiple subcellular pools.
354
355 Our experiments demonstrate that FACES is an especially powerful tool for investigating cellular
356 mechanisms by which lipids are transported between organelles and across individual
357 membranes, an intense area of investigation. A plethora of shuttle and bridge-like LTPs that
358 perform lipid exchange at contact sites[54] and flippases/floppases/scramblases that act on bilayer
359 asymmetry[55] have been identified and biochemically tested. However, these transporters are
360 characterized by overlapping affinities, apparent redundancies, and close interactions with lipid
361 metabolic enzymes; how they act in concert to shape the membrane heterogeneity that defines
362 eukaryotic cells is still unknown. Here, we show that FACES can report the asymmetry of
363 several labeled phospholipid classes in post-Golgi vesicles. The Golgi has long been proposed
364 as a site of asymmetry generation, given the co-occurrence of secretory cargo sorting to the PM
365 and sphingolipid synthesis[56]. Golgi membranes also host phospholipid flippases; genetic and
366 biochemical studies in yeast have suggested that TGN vesicle budding is tied to the generation
367 of lipid asymmetries by P4-ATPase that flip phospholipids[57]. Vesicles that are defined by
368 phospholipid asymmetry are enriched in GPI-anchored secretory cargoes that associate with

369 the exoplasmic leaflet of the PM, consistent with these models. Lipid asymmetry generated at
370 the TGN could also be required to sort transmembrane proteins based on the asymmetric TMD
371 sequences that are required for PM targeting[3,58]. As a tool that provides spatially-defined
372 molecular quantitation, FACES could be broadly powerful for untangling how lipid trafficking,
373 generation of membrane asymmetry, and transport of cargoes occurs throughout eukaryotic
374 cells.
375

376 **Acknowledgements**

377

378 Gulcin Perkunnaz provided helpful discussions and reagents, Jennifer Santini and the UCSD
379 Microscopy Core (NS047101, OD030505) provided assistance with microscopy, Chris Burd and
380 Jennifer Lippincott-Schwartz provided plasmids. The work was supported by the National
381 Institutes of Health (R35-GM142960 to I.B. and R35GM141939 to N.K.D.) and the National
382 Science Foundation (CHE-2310263 to M.D.B.). R.J.B. acknowledges Agencia Estatal de
383 Investigación and the Ministerio de Ciencia e Innovación (RYC2020-030065-I).
384

385 **Methods**

386

387 Synthesis of fluorogen reagents: Synthesis schematic of compounds **1a** and **1b** are shown in
388 Supplementary Fig. 1b and synthetic protocols are detailed in the Supplementary Text. Products
389 were validated by LC-MS and $^{1}H/^{13}C$ NMR.
390

391 Generation of constructs: FAPs were cloned from pcDNA3.1-KozATG-dH6.2-2XG4S-actin[15],
392 pcDNA3.1-kappa-myc-dK-2xG4S-TMst[59], and pcDNA3.1-kappa-myc-dL5-2XG4S-mCer3-
393 KDEL[60] (Addgene). These FAP sequences and the pcDNA3.1 backbone were used for
394 generating the FAP-GFP-KDEL, GFP-KDEL, and MTS-FAP-GFP constructs used in transfection

395 experiments (Fig. 2). The Ig Kappa secretion signal was used in conjunction with a KDEL
396 sequence for ER-targeted constructs, while the targeting sequence from OTC was used for
397 MTS constructs. For stable expression, FAP-GFP-KDEL and MTS-FAP-GFP coding sequences
398 were subcloned into the sleeping beauty expression vector SBbi-PUR[61] (Fig. 3, Fig. 5).
399 Constructs utilizing TGN38 were derived from mCer3-TGN38, which was a gift from the
400 Lippincott-Schwartz lab. In transfection experiments, the dH6.2 sequence was inserted into
401 either the N-terminal or C-terminal side of the TGN38 transmembrane domain to generate
402 mCer3-FAP-TGN38 and mCer3-TGN38-FAP constructs, respectively (Fig. 4d, Supplementary
403 Figures 7 and 10). For stable cell lines, a reciprocal tagging approach was taken to generate
404 FAP-TGN38-GFP and GFP-TGN38-FAP constructs assembled into the SBtet-Pur expression
405 vector (Fig. 4b-c, Supplementary Fig. 8). The GPI-anchor marker protein was generated by
406 subcloning a mCherry-SBP-GPI sequence, received from the Lippincott-Schwartz lab, into
407 pcDNA3.1. The GFP-EqtSM plasmid was received as a gift from the Burd lab. Additional
408 Sec61mCherry and Mito-BFP plasmids were received from the Lippincott-Schwartz lab. All
409 constructs were validated by whole plasmid sequencing.
410
411 Cell culture: HeLa (ATCC CCL-2) cells were grown in Dulbecco's Modified Eagle Medium
412 (Gibco 11995-065) containing glucose (4.5 g/L), glutamine (4.5 g/L), sodium pyruvate (110
413 mg/L), phenol red, 10% FBS, and 1% PenStrep, at 37°C and 5% CO_2 atmosphere. For
414 microscopy, cells were seeded into 35 mm glass bottom dishes (MatTek) coated with fibronectin
415 (7.5 µg/mL). For transient expression, cells were transfected with Lipofectamine 3000 in
416 Opti-MEM media for 4 h, and changed into normal growth medium containing azido-containing
417 bioorthogonal metabolite for 24 h prior to SPAAC labeling and imaging. Stable cell lines
418 expressing FAPs were generated using the Sleeping Beauty transposon insertion system. After
419 transfection, cells were grown under selection with puromycin (10 µg/mL) for 2 weeks until all
420 showed fluorescence. Cells were routinely tested for mycoplasma by MycoStrip (InvivoGen).

421

422 Metabolic labeling: 1-azidoethyl-choline (N_3-Cho, Jena BioScience) and resuspended in PBS to
423 stock concentration of 50 mM. Ac_4ManNAz, Ac_4GalNAz and Ac_4GlcNAz (Click Chemistry Tools)
424 were resuspended in DMSO to stock concentration of 100 mM. L-Serine analogue C-L-Ser-N_3
425 and *myo*-Inositol analogue Inos-N_3 were synthesized as previously reported, verified by ^{1}H/^{13}C
426 NMR and high resolution mass spectrometry, and resuspended in PBS to a stock concentration
427 of 50 mM and 100 mM, respectively. In all cases, metabolic incorporation occurred for 24 h.
428 Afterwards, cells were washed once with HBSS buffer, and incubated in fresh growth media for
429 30 min to allow for metabolic consumption of any remaining bioorthogonal metabolites. For
430 experiments with peracetylated sugars, 1 h incubation was used.

431

432 SPAAC conjugation: Culture media was removed by aspiration and replaced with staining media
433 for SPAAC labeling. The staining media contained 500 nM **1a** or **1b** diluted in serum-free DMEM
434 clear (Gibco 31053-028), and incubated for 15-20 min at 37°C and 5% CO_2 atmosphere. Cells
435 were washed with 4 volumes of culture media containing 10% FBS, 3 times, at 15 min intervals
436 to remove unreacted dye. For experiments with the mitochondrial-localized FAP, cells were
437 incubated for an additional 45 min, followed by a fourth wash step prior to imaging.

438

439 Lipid analysis: Lipids were extracted with a modified Bligh and Dyer protocol. Briefly, cell pellets
440 from T75 culture flasks were resuspended in 200 µL PBS and extracted with 2 mL 1:2
441 $CHCl_3$:MeOH (v/v) and cell debris were removed by centrifugation. Extracts were transferred to
442 new vials and 1 mL chloroform was added, followed by 1 mL H_2O, and shaking. The lower
443 organic phase was collected after centrifugation and the aqueous phase was extracted twice
444 more with 650 µL and pooled. Lipid extracts were then dried under N_2 and resuspended in 100
445 µL 1:2 $CHCl_3$:MeOH for thin-layer chromatography (TLC) and 500 µL methanol for LC-MS/MS.
446 For TLC, entire lipid extracts were spotted onto 10x10 cm HPTLC silica gel 60 plates,

447 developed with 14:5:1 $CHCl_3$:MeOH:NH_4, and imaged with a Typhoon FLA 9500 using 633 nm
448 laser. For LC-MS/MS, 5 µL sample was injected, andHRMS spectra of the total lipid extracts
449 from HeLa cells were recorded on a Q Exactive Orbitrap mass spectrometer (Thermo Fisher
450 Scientific) connected to a Vanquish Flex Analytical UHPLC System (Thermo Fisher Scientific)
451 equipped with a C8 column (100 x 2.1 mm, particle size 1.9 µm). Following HPLC method was
452 used for all runs using 0.1% formic acid in water (Solvent A) and 0.1% formic acid in methanol
453 (Solvent B): 0-1 min 30% B, 1-4 min 30%-90% B, 4-15 min 90-99% B, 15-18 min 99%B, 18-20
454 min 30% B. Lipid standards (POPC, N_3-DSPC) were supplied by Avanti Polar Lipids.
455
456 Image collection: Confocal micrographs were acquired on a Zeiss LSM 880 microscope
457 equipped with plan-apochromat 64x/1.4 NA or 20x/0.8 NA objectives. For far-red fluorogen-FAP
458 signals, a 633 nm HeNe laser was used at 1-2% power. FP or other fluorophores were excited
459 with 488 nm Argon (GFP), 405 nm (BFP/mCer3) or 561 nm (mCherry) diode lasers. All images
460 used for intensity quantification were acquired in LSM mode using a QUASAR GaAsP detector
461 using identical settings. SIM imaging of mitochondrial **1b**-PC was performed on an Zeiss Elyra 7
462 Lattice-SIM^2 system equipped with a plan-apochromat 100x/1.46 NA objective using 642 nm
463 and 488 nm diode lasers (10% power each). Images were acquired in ZEN Black using Weak
464 Live default settings with a pixel dwell time of 843 ms.
465
466 Image quantification: All intensity were calculated using ImageJ on unprocessed images. For
467 proof of concept experiments using transfected cells (Fig. 2), line profiles drawn were across 10
468 individual ER segments per cell and the total fluorescence ratio between fluorogen and GFP
469 emissions were tabulated across them. For per-cell data (Fig. 2d, 2f), the 10 segments were
470 averaged and 10 cells were analyzed per condition. Raw per segment fluorescence intensity is
471 shown for all 100 segments in Fig. 2e. For mitochondrial and ER quantification in Fig. 3, fields of
472 cells stably expressing to corresponding FAPs were analyzed by segmenting individual cells

473 and computing the total fluorescence ratio between fluorogen and GFP emission across the
474 entire cell, given the highly specific distribution of the signal for the compartment of interest. For
475 TGN cisternae quantification (Fig. 4, 5), line segments were drawn across the Golgi apparatus
476 of individual cells so that they did not intersect any TGN vesicles. For TGN vesicle
477 quantification, 5 line segments were drawn across Golgi vesicles that did not intersect Golgi
478 cisternae. For each compartment, the total fluorescence ratio between fluorogen and GFP were
479 calculated across each and averaged together for a single cell value. Values were measured
480 this way for 25 cells per condition (luminal vs. cytosolic for PC, PS, PI, and SiA). Mitochondrial
481 quantification in Fig. 5 was carried out identically as in Fig. 3. Images highlighting fluorogen
482 distribution (Figs. 2a, 2b, 3a, 3b, 4b, 4d; Supplementary Figs. 3a, 3b, 7, 9, 10; Supplementary
483 Movies 1, 2) were acquired with an Airyscan detector and processed using default settings in
484 Zen Black; these were not used for quantification due to non-linear processing. All statistical
485 analyses were performed in GraphPad Prism 9.
486
487 Gene knockdown: Pre-validated Silencer Select siRNAs were supplied by Thermo Fisher:
488 STARD7 (s32370), VPS13a (s531256), negative control 1 (4390843). Cells were transfected
489 with Lipofectamine RNAiMAX (ThermoFisher) complexed with 25 pmol siRNA for 48h prior to
490 analysis. Total protein was extracted using RIPA Lysis and Extraction buffer (ThermoFisher) and
491 measured by Bradford assay (Bio-Rad). A total 20 µg protein per extract was boiled in 1X
492 reducing sample buffer and used for SDS-PAGE (BioRad, 4561083). Validation of gene
493 knockdowns was performed by Western blotting using primary antibodies against STARD7
494 (Proteintech, 15689) 1:2500, VPS13a (Atlas antibodies, HPA021662) 1:1000, and Actin
495 (Invitrogen, PA5-78715) 1:5000. HRP-conjugated goat anti-rabbit IgG secondary antibody
496 (Abcam, 6721) 1:10,000 and Pierce ECL western blotting substrate (Thermo Fisher, 32209)
497 were used for detection.
498

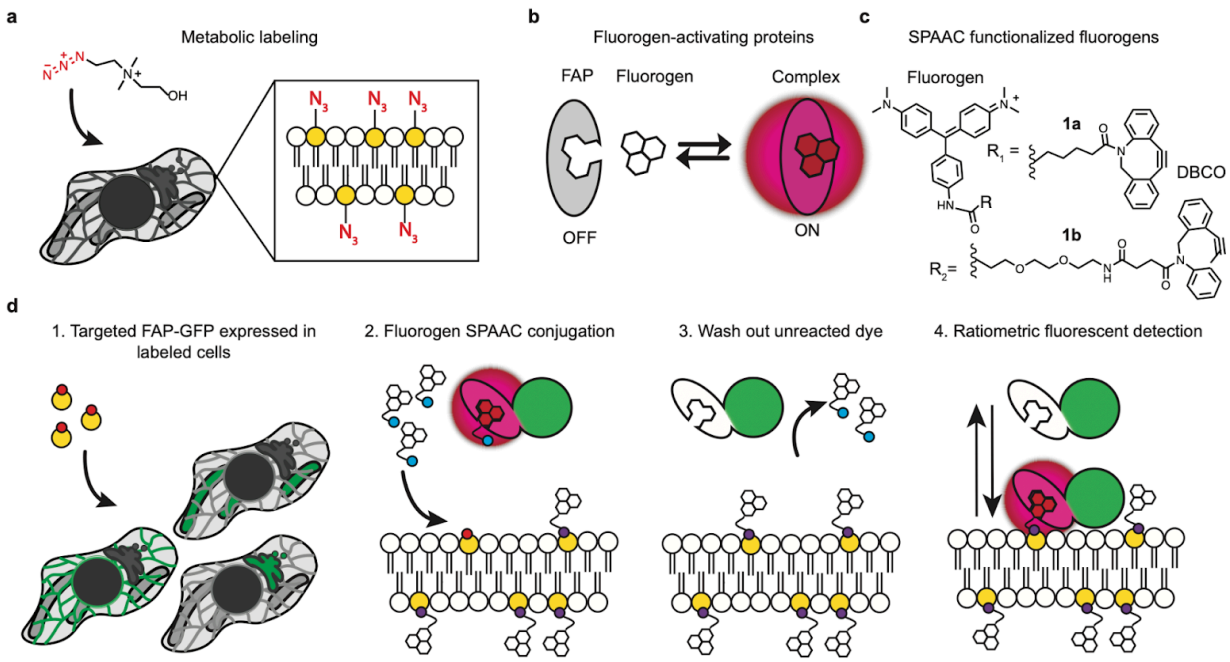

Figure 1. Conceptual development of FACES

a, N_3-Cho is metabolically incorporated into azido-PC lipids distributed throughout all cellular membranes. **b,** Fluorogens form reversible non-covalent fluorescent complexes with genetically encoded FAPs. **c,** Structure of the fluorogen malachite green linked to dibenzocyclooctyne for SPAAC labeling. **d,** Conceptual schematic detailing the FACES method. (1) Cells expressing a FAP-GFP fusion protein targeted to an organelle of interest are metabolically labeled with N_3-Cho, or other bioorthogonal metabolite. (2) After incorporation, metabolites are conjugated via a SPAAC reaction with fluorogen-DBCO. During this time free dye can interact with the FAP to generate far-red fluorescence. (3) After SPAAC labeling, excess free dye is reversibly disassociated from the FAP complex and removed from cells by washing. (4) Subsequent imaging of the fluorogen-FAP complex is used to detect the specific biomolecule pool. Co-measurement of GFP fluorescence is used to normalize the fluorogen signal to FAP sensor density.

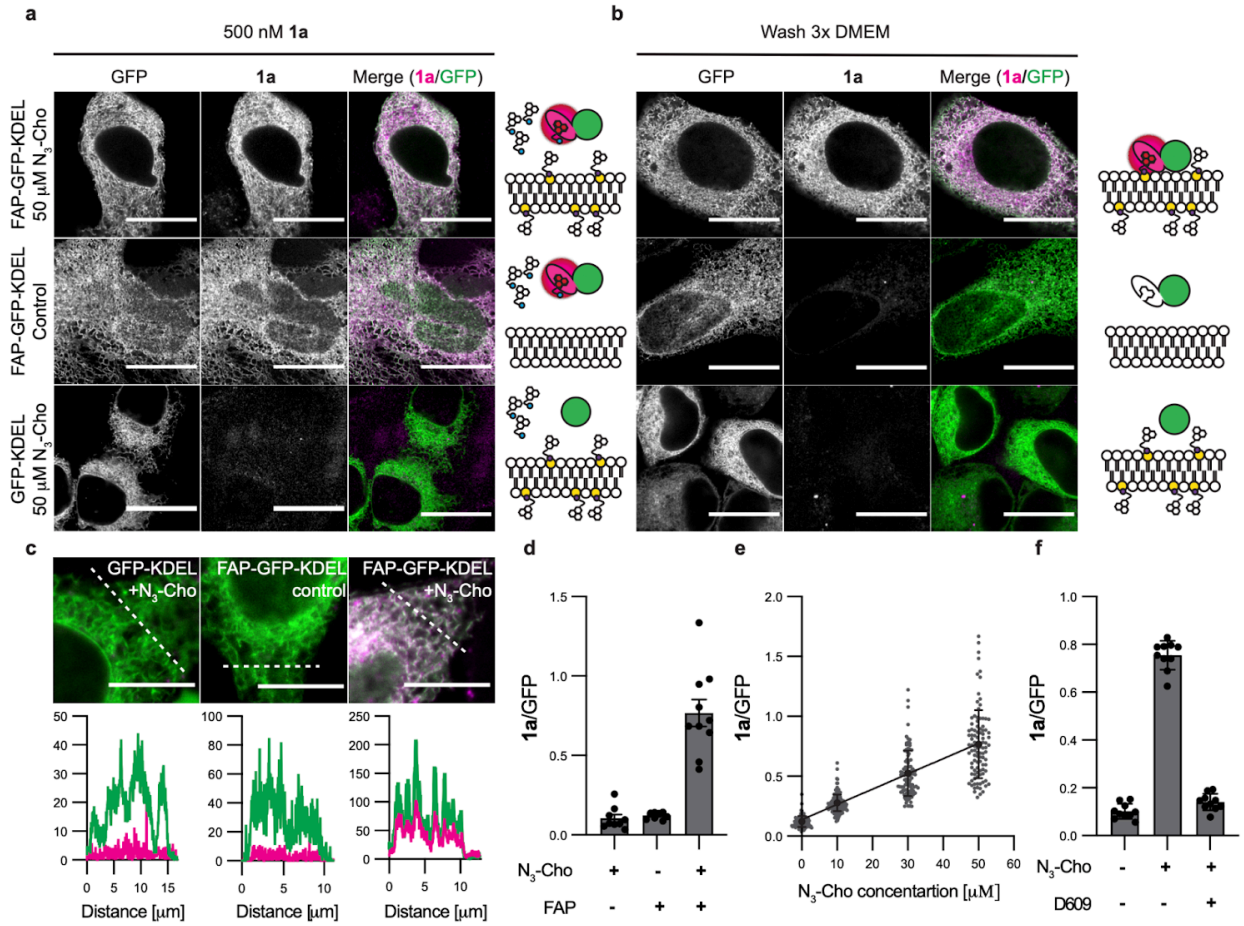

Figure 2. Imaging N_3-PC in the ER using compound 1a

a, b, HeLa cells transfected with either FAP-GFP-KDEL (top two rows) or GFP-KDEL (bottom row) were grown in the presence (top and bottom rows) or absence (middle row) of 50 μM N_3-Cho and labeled with 500 nM **1a**. Cells were imaged while in the labeling solution **(a)** and after washing with culture medium **(b)**. In washed cells, fluorgen fluorescence is only visible when both N_3-PC and the FAP domain are present, while in unwashed cells unreacted fluorogens also fluoresce. Scale = 20 μm. **c,** Merged confocal images of transfected HeLa cells post washing. White line indicates the segment used for plotting the fluorescent intensity profile of **1a** and GFP shown below. Scale = 10 μm. **d,** Quantified fluorescence intensity profiles from confocal images expressed as ratiometric average; *n* = 10 cells. **e,** Linear regression of quantified fluorescence from transfected HeLa cells fed 0, 10, 30, 50 μM N_3-Cho and labeled with 500 nM **1a**; *n* = 100 individual ER segments derived from 10 cells. **f,** Quantified fluorescence of cells incubated with the PC synthesis inhibitor D609 alongside N_3-Cho; *n* = 10 cells.

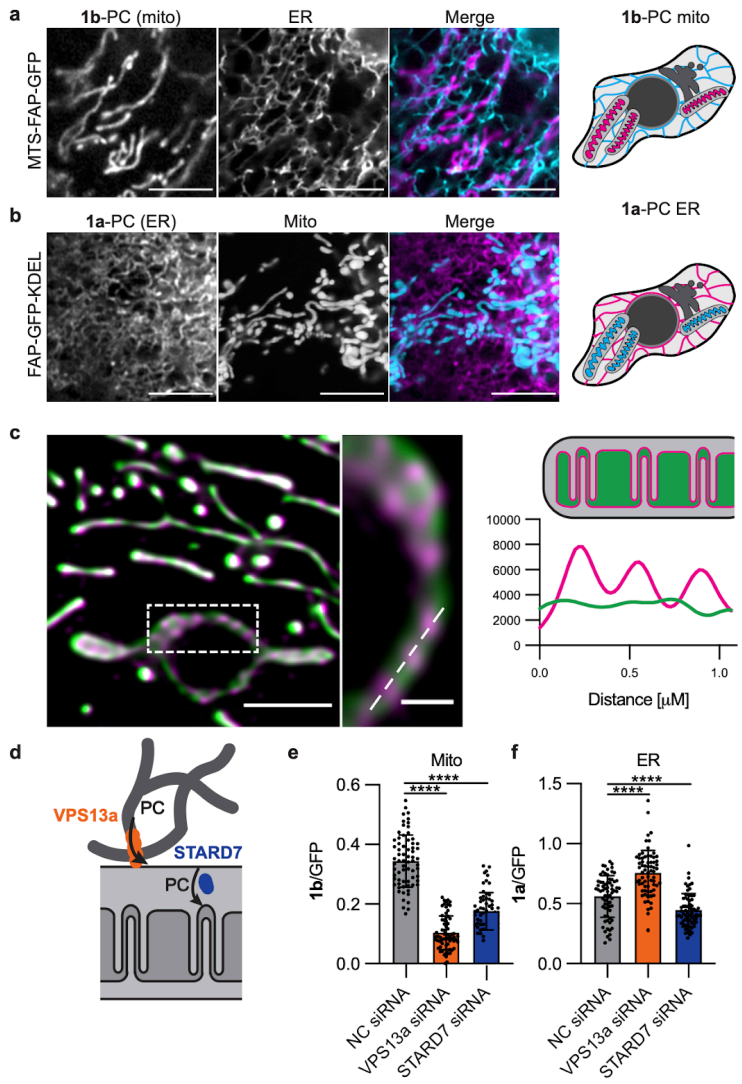

Figure 3. Using FACES to analyze PC trafficking between the mitochondrion and the ER

a, HeLa cells co-transfected with an ER-localized FAP (FAP-GFP-KDEL) and a mitochondrial marker (mito-BFP) show fluorogen fluorescence in the far-red channel that does not overlap with mitochondria. **b,** HeLa cells co-transfected with a mitochondrial matrix FAP (MTS-FAP-GFP) and an ER marker (Sec61-mCherry) show fluorgen fluorescence that does not overlap with the ER. For both **(a)** and **(b)**, 50 μM N_3-Cho and 500 nM **1a** were used for PC labeling. Scale = 5 μM. **c,** Super-resolution live cell imaging of **1b**-PC (magenta) in the mitochondrial matrix with Elyra 7 lattice SIM[2]. The graph below indicates fluorescence intensity profiles of **1b**-PC (magenta) and GFP (green) along the white dashed line (inset). Scale = 2 μm and 0.5 μm, respectively. **d-f,** Knockdown of two putative ER-mitochondrial lipid transporters alters the distribution of PC between the two organelles. Stable cell lines expressing

541 MTS-FAP-GFP **(e)** and FAP-GFP-KDEL **(f)** were used to quantify N_3-PC levels in the
542 mitochondrion (Mito) and ER, respectively; *n* = 70 cells per condition; ***, $p < 0.01$. Images
543 corresponding to each condition are shown in Supplementary Fig. 5a.

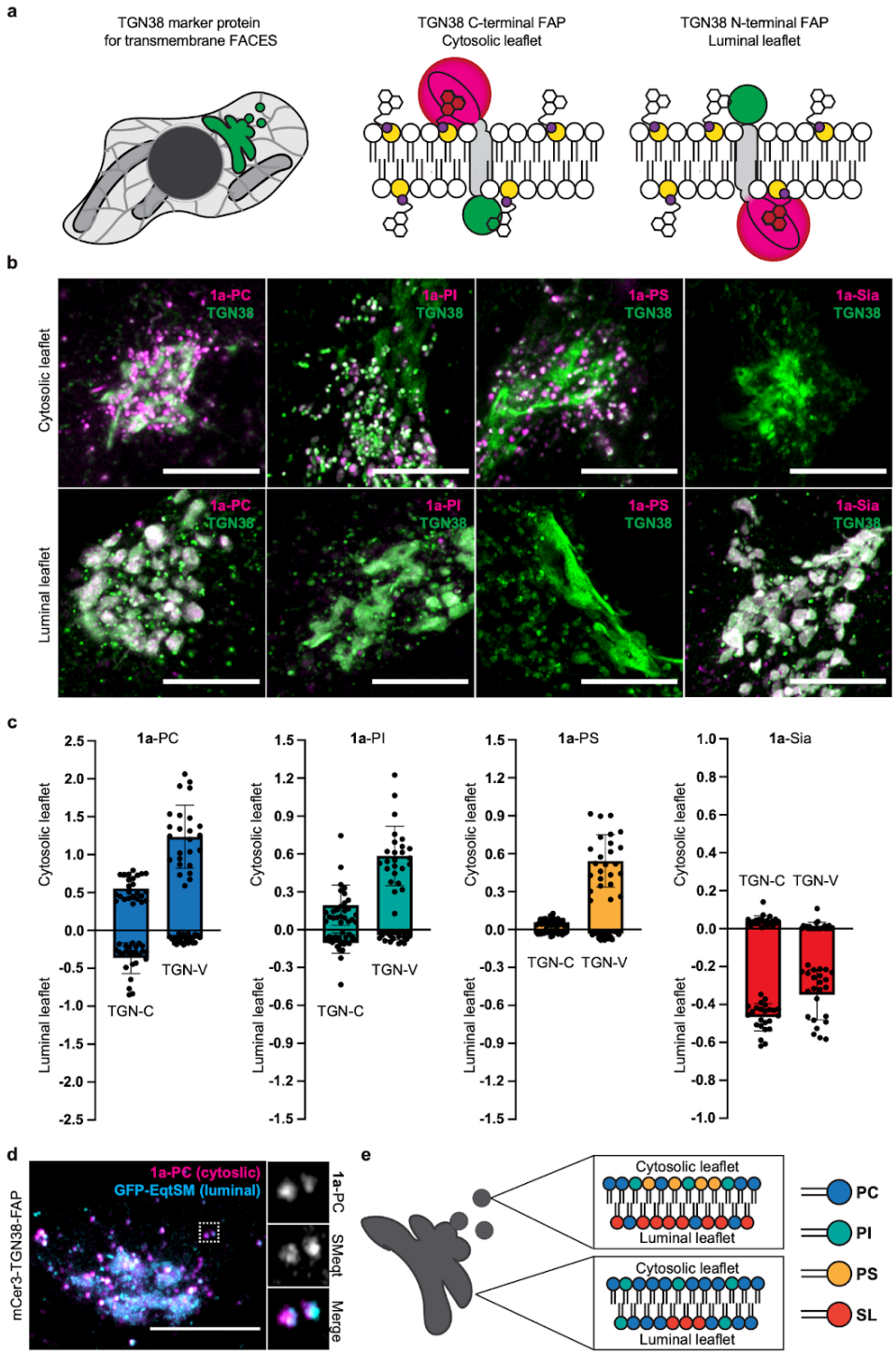

Figure 4. Imaging lipid asymmetry generated at the TGN with FACES

a, Illustrated schematic representing the constructs used for reciprocal tagging of TGN38 with a FAP exposed to the cytosolic or luminal leaflet. The constructs also include the cyan fluorescent protein mCer3 on the opposing leaflet to account for sensor abundance. **b,** Example composite images of individual Golgi from HeLa cells stably expressing the cytosolic (top) or luminal

(bottom) TGN38 FAP sensors. Cells were treated with a tracer for PC (100 μM N_3-Cho), PI (50 μM Inos-N_3), PS (250 μM C-L-Ser-N_3), or Sia (50 μM Ac_4ManNAz). Images were acquired using 441 nm and 633 nm laser lines. Magenta regions are enriched in the fluorogen conjugated metabolite, green regions correspond to low metabolite levels, while white regions show intermediate values, relative to the sensor levels. **1a**-PC detection in the TGN using 100 μM N_3-Cho and 500 nM **1a**. Scale bar = 10 μm. **c**, Quantification of the fluorescence intensity ratio of fluorogen to mCer3 for each metabolite and each orientation (cisternae, TGN-C; vesicles, TGN-V). Values were calculated post-subtraction of the background fluorescence using unfed null controls. Error bars indicate SD; *n* = 25 cells per metabolite per leaflet. Raw values and statistical analyses are provided in Supplementary Fig. 7. **d**, Co-localization of SMeqt-GFP and cytoplasmic **1a**-PC in individual TGN vesicles, as detected by mCer3-TGN38-FAP. Here, 488 and 633 nm laser lines were used for imaging to avoid imaging of mCer3. The SMeqt-GFP channel is colored cyan and the **1a**-PC channel is colored magenta. Scale = 10 μm. **e,** Conceptual model representing the proposed asymmetric distribution of PC and SM lipids that is generated alongside TGN vesicle formation.

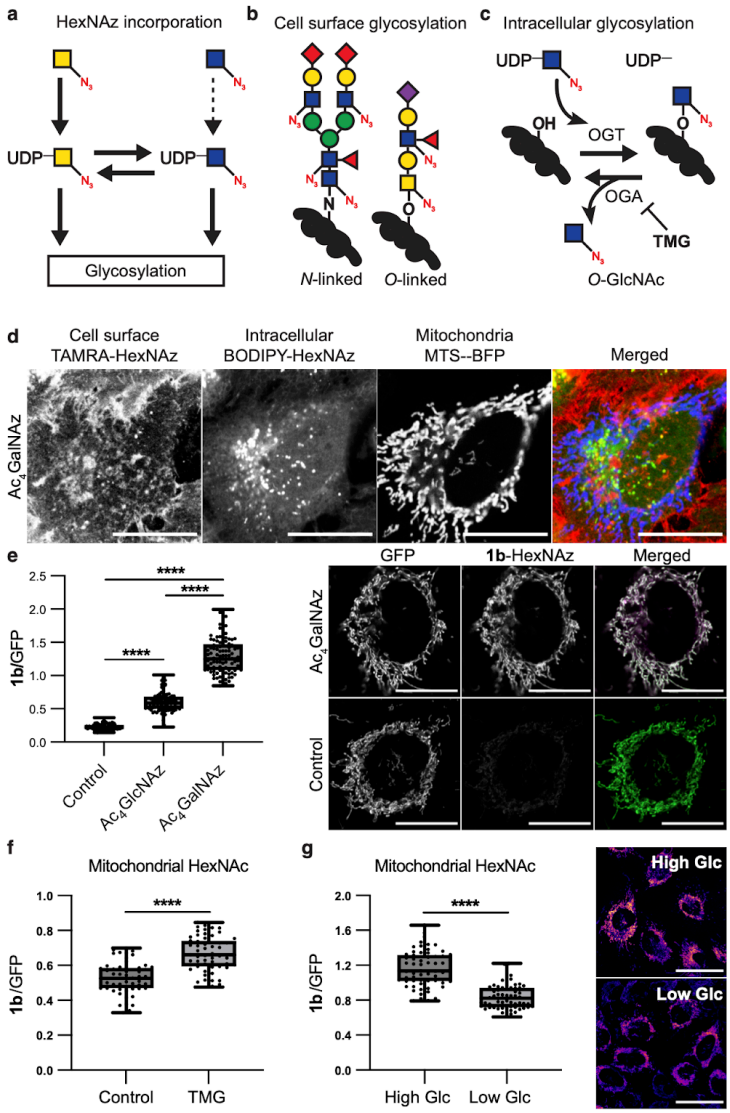

Fig. 5. Intracellular imaging of *N*-acetylhexosamine sugars with FACES

a, Illustration depicting the metabolic fate of Ac_4GalNAz (yellow square) and Ac_4GlcNAz (blue square) incorporation into cellular glycoconjugates containing *N*-acetylhexosamine sugars. Ac_4GalNAz fed to cells is converted to UDP-GalNAz in the cytosol and further epimerized to UDP-GlcNAz, thereby robustly labeling both UDP-HexNAz pools (UDP-GalNAz + UDP-GlcNAz). Conversely, Ac_4GlcNAz is not efficiently recycled to UDP-GlcNAz. **b**, UDP-HexNAz is incorporated into diverse extracellular glycoproteins proteins on the cell surface. Structures for an *N*-linked glycoprotein and *O*-linked mucin are shown as examples. **c**, UDP-HexNAz is incorporated into intracellular *O*-GlcNAcylated proteins. Protein glycosylation is catalyzed by *O*-GlcNAc Transferase (OGT) and can be reversed by *O*-GlcNAcase (OGA). OGA

is pharmacologically inhibited by Thiamet-G (TMG). **d,** Bioorthogonal imaging of HeLa cells fed 100 μM GalNAz for 24h and labeled with 5 μM TAMRA-DBCO (cell surface) and 5 μM BODIPY-DBCO (intracellular), relative to the mitochondrial marker Mito-BFP. Scale = 20 μm. **e-i**, Stable MTS-FAP-GFP cells detect mitochondrial HexNAz. **e**, Quantified mitochondrial HexNAz incorporation in cells fed either 100 μM Ac_4GalNAz or 100 μM Ac_4GlcNAz for 24h, versus unfed controls. Error bars indicate SD; *n* = 100 cells. Cells were labeled with 500 nM **1b** and washed as previously described. Representative images of Ac_4GalNAz fed cells and control are shown on the right; scale = 20 μM. **f**, Response of mitochondrial HexNAz to OGA inhibition using Thiamet-G (TMG). Cells were treated with 50 μM Thiamet-G (or DMSO control) and fed 100 μM Ac_4GalNAz for 24h. Displayed values are normalized to the average background fluorescence of unfed cells, which were used to control for **1b** labeling. Error bars indicate SD; *n* = 59 cells. **g**, Response of mitochondrial HexNAz to glucose availability. Cells were fed 100 μM Ac_4GalNAz and grown in DMEM containing either low (5.5 mM) or high (30 mM) glucose for 24h. Displayed values are normalized to unfed cells used as control for **1b** labeling. Error bars indicate SD; *n* = 63 cells. Representative LSM images (right) show **1b**-HexNAz fluorescent intensities displayed using the FireLUT. Scale = 50 μm.

Supplementary Figures

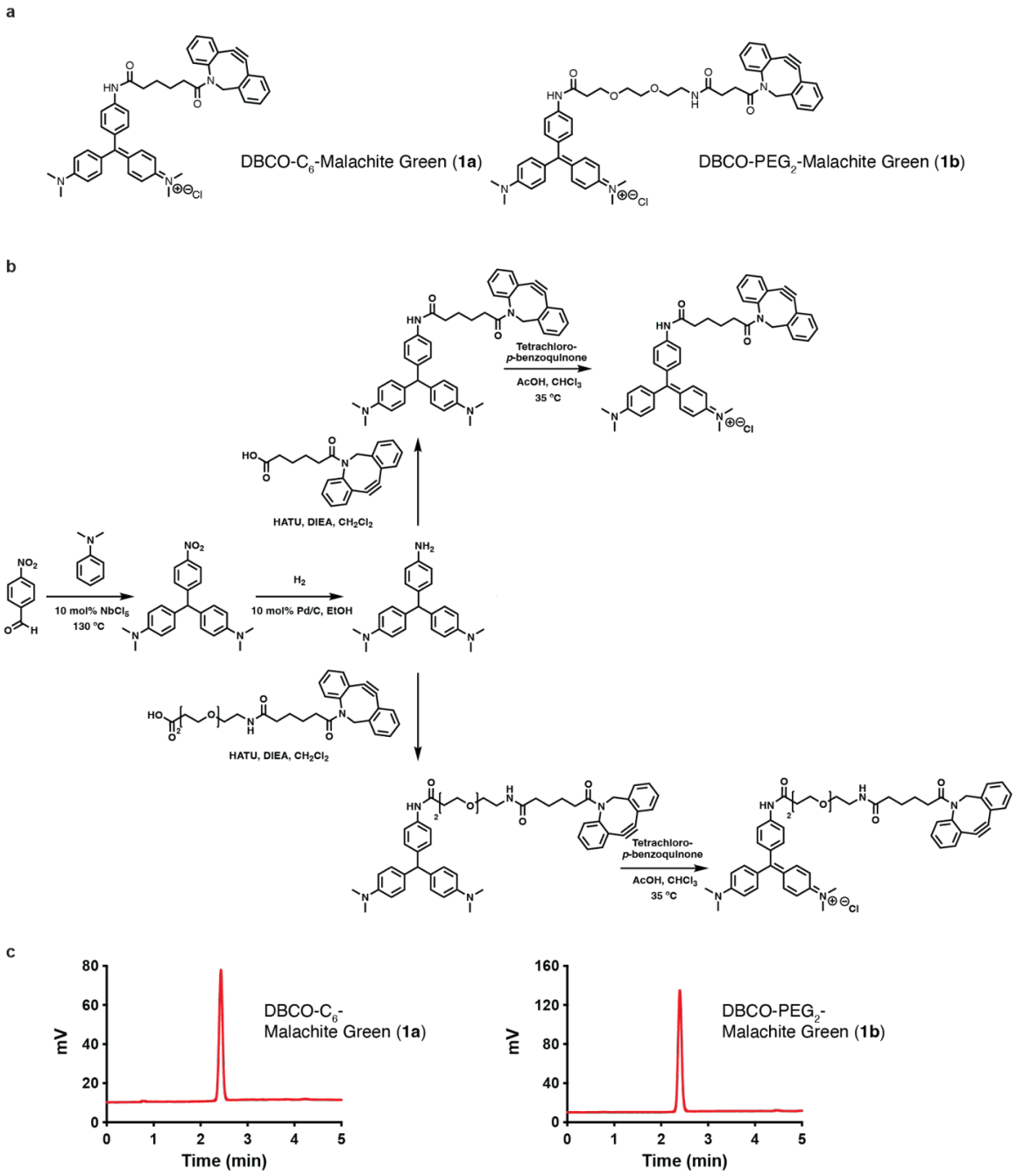

Supplementary Fig. 1. Synthesis of DBCO-linked fluorogens

a, Chemical structures of all the Malachite Green (Chromatic forms) derivatives used in this study. **b**, Synthesis of the chromatic forms of DBCO-C_6-Malachite Green (**1a**) and DBCO-PEG_2-Malachite Green (**1b**). **c**, HPLC/ELSD spectrum corresponding to the chromatic forms of DBCO-C_6-Malachite Green (**1a**) and DBCO-PEG_2-Malachite Green (**1b**). Retention times were verified by mass spectrometry.

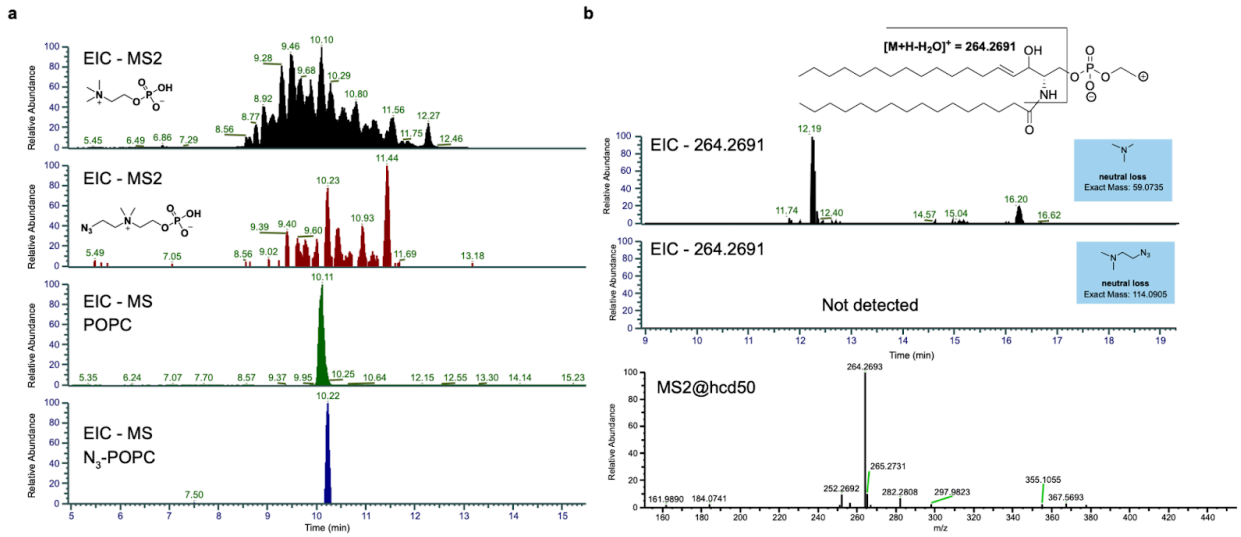

Supplementary Fig. 2. N_3-Cho is metabolized into N_3-PC but not N_3-SM

Cells were fed 100 μM N_3-Cho for 24 h and extracted lipids were analyzed by LC-MS/MS. **a**, Comparative extracted ion chromatograms (EIC) from full scan/all ion fragmentation mode. MS2 fragments: choline (black), N_3-Cho (red). EIC of POPC (green) and N_3-POPC (blue) were detected as representative PC species in the sample. **b**, Sphingoid base fragment 264.269 was detected in neutral loss scan mode NL = 59 (choline containing lipids) but not in NL = 114 (N_3-Cho containing lipids), indicating N_3-Cho was not incorporated into SM in a detectable amount under these labeling conditions.

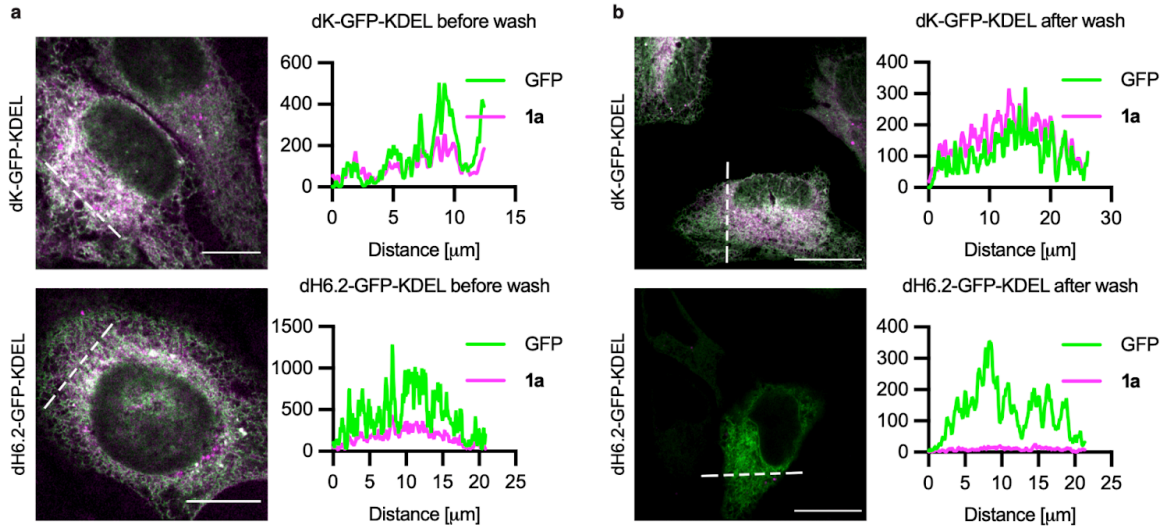

Supplementary Fig. 3. 1a-FAP complex reversibility depends on the heavy chain scFvs FAP clone dH6.2

Cells that were not fed with any azido metabolites were transfected with either dH6.2-GFP-KDEL or light chain scFvs FAP variant dK-GFP-KDEL and stained with 500 nM **1a**. dH6.2 was shown to have reversible binding to MG[15,59], while dK features nanomolar affinity[15,59] and is thus irreversibly bound under experimental conditions. **a**, Cells imaged while in staining solution show co-localization of sensor (GFP) and fluorogen (**1a**) signal for both constructs. Scale = 10 µm. **b**, Cells imaged after washing 3x with DMEM show only fluorogen signal for the dK construct (top), as FAP-bound 1a is not washed out. Line profiles show the relative change in **1a** fluorescence intensity compared to GFP. Specific detection of SPAAC-conjugated fluorogens thus requires a lower affinity FAP like dH6.2. Scale = 25 µm.

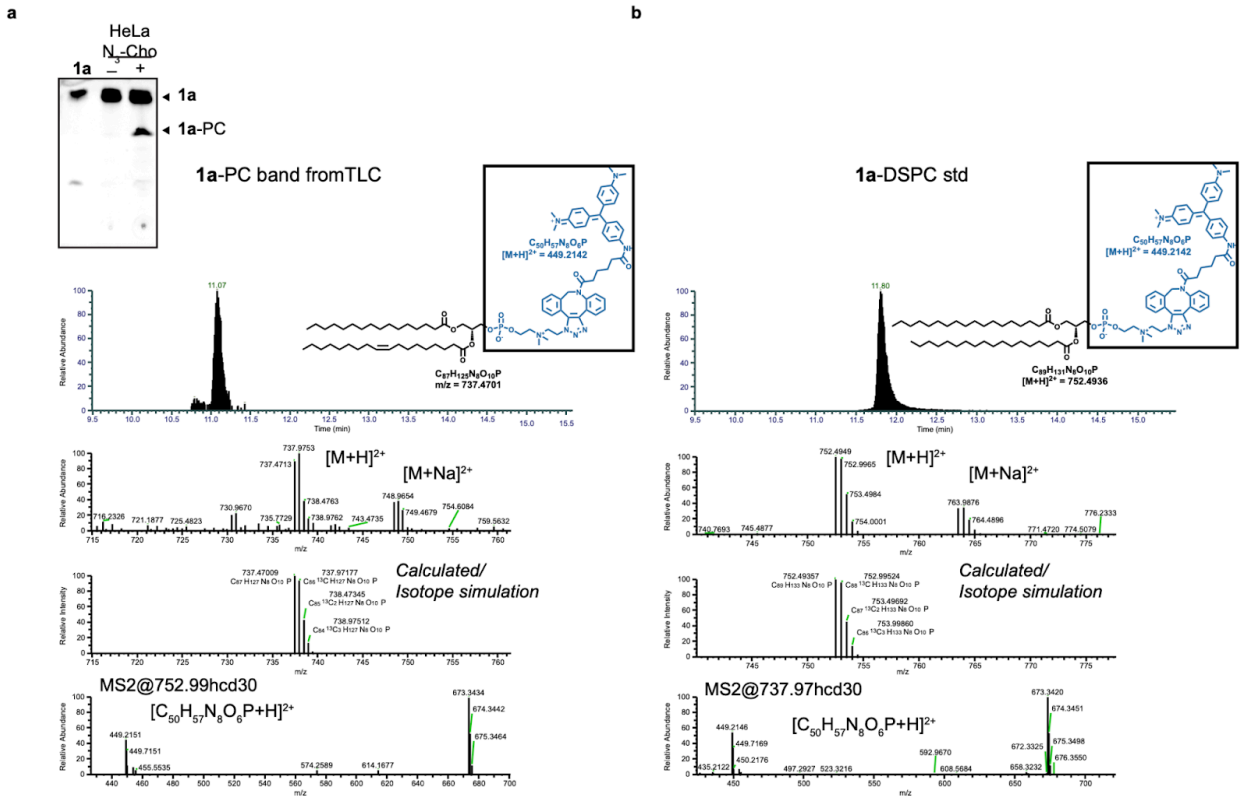

Supplementary Fig. 4. 1a-PC conjugates are formed in cells

a, HR-MS/MS analysis of **1a**-PC band from thin layer chromatography detecting $[M+H]^{2+}$=747.4713 and MS2 fragment 449.2146. Cells stained with **1a** were not washed prior to lipid extraction to highlight conversion of **1a** to **1a**-PC. **b**, Comparative HR-MS/MS analysis of the **1a**-DSPC standard previously synthesized by reaction of **1a** with N_3-DSPC detecting $[M+H]^{2+}$=752.4949 and MS2 fragment 449.2146.

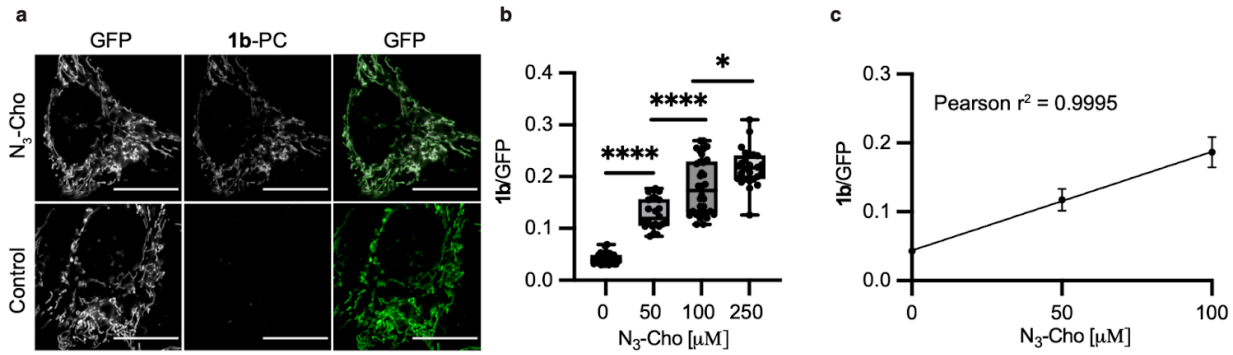

Supplementary Fig. 5. Linear quantification of 1b-PC in the mitochondrial matrix

a, HeLa cells stably expressing MTS-FAP-GFP were fed different concentrations of N_3-Cho for 24h and stained with 500 nM **1b**. Images show that fluorogen fluorescence (middle) is dependent on azido metabolic incorporation. Scale = 20 μm. **b**, Quantification of **1b**/GFP fluorescence in cells expressing MTS-FAP-GFP with increasing concentrations of N_3-Cho. **c**, Linear increase of **1b**/GFP fluorescence only up to 100 μM N_3-Cho.

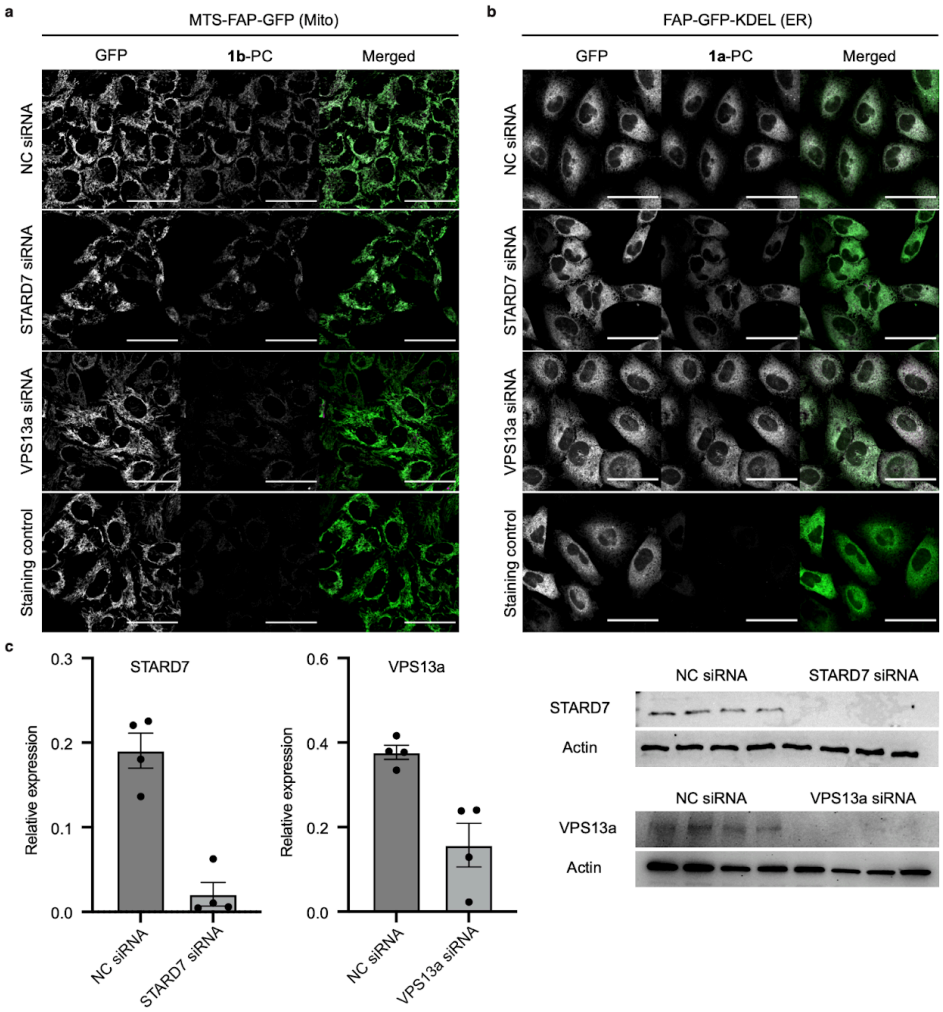

Supplementary Fig. 6. LTP silencing affects 1a-PC abundance in the mitochondria and ER **a-b**, Representative LSM images of siRNA transfected cells stably expressing either MTS-FAP-GFP **(a)** and FAP-GFP-KDEL **(b)** Null control (NC) siRNA shows robust **1a**-PC/**1b**-PC signal in both compartments. Both STARD7 and VPS13a show reduction in mitochondrial **1b**-PC signal, but only VPS13a knockdown shows a concomitant increase in ER **1a**-PC signal. Scale = 50 µm. **c**, Silencing efficiency of the two siRNAs compared to the NC as determined by western blotting.

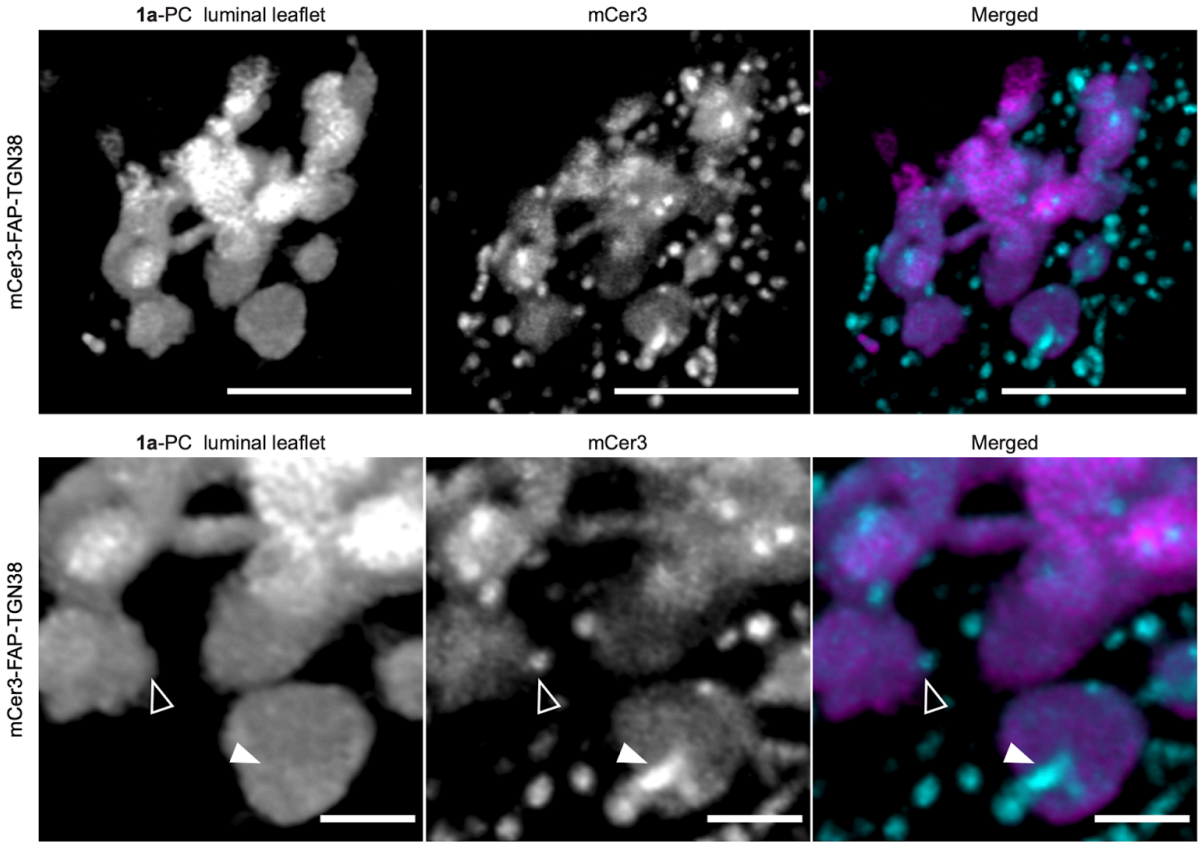

Supplementary Fig. 7. TGN vesicle formation is associated with a loss of luminal PC Golgi (top) and highlighted region (bottom) are shown from an individual cell were transfected with mCer3-FAP-TGN38, fed 100 μM N_3-Cho for 24h, and labeled with 500 nM **1a**. 3D rendering of Airyscan z-stacked images show a lack of **1a**-PC labeling on the luminal leaflet of vesicles (arrow, outline) and tubes (arrow, filled) connected to TGN cisternae. Airyscan images were acquired with 405 and 633 lasers for excitation and localization of mCer3 and **1a**-PC, respectively. Scale = 10 μm (top) and 2 μm (bottom).

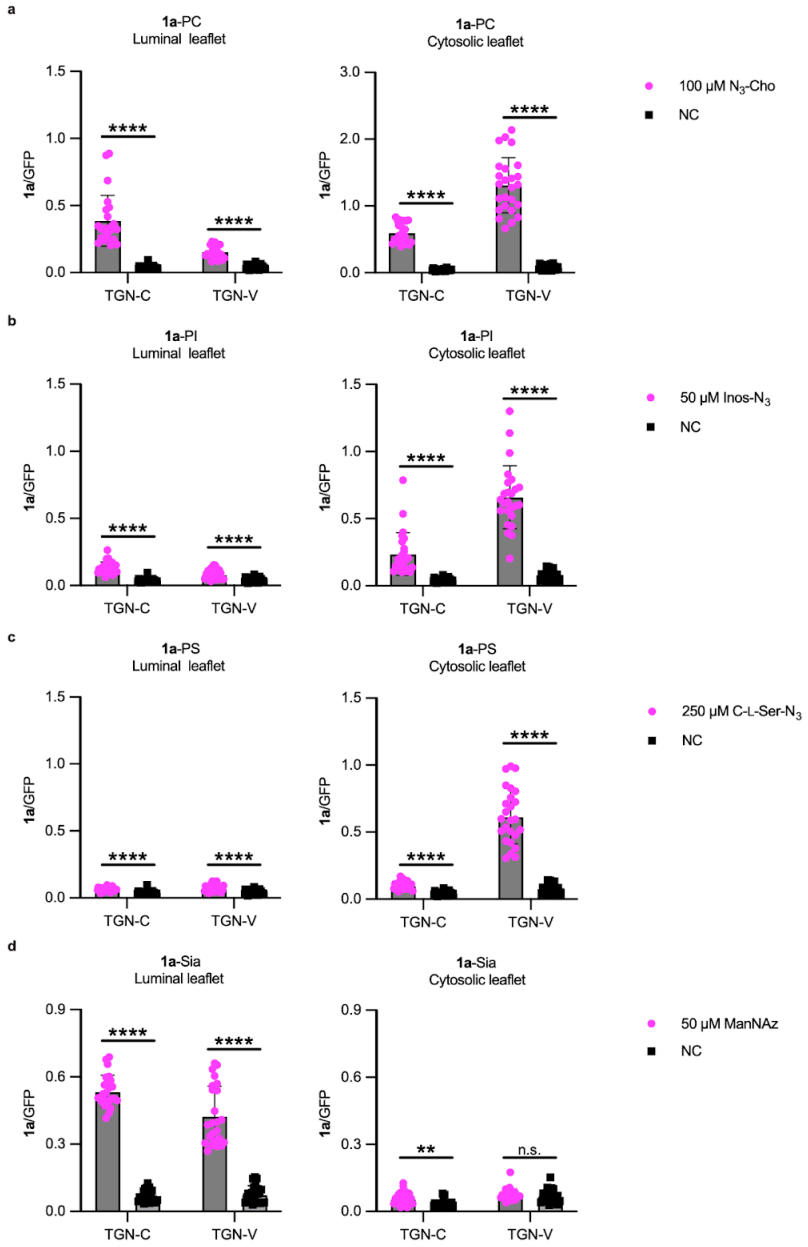

Supplementary Fig. 8. FACES quantification of phospholipid asymmetry across the TGN Cells stably expressing Tet inducible FAP-TGN38-GFP (luminal leaflet) or GFP-TGN38-FAP (cytosolic leaflet) constructs were grown under 1 μg/mL doxycycline and fed different azido metabolic labeling reagents for 24h prior to staining with 500 nM **1a**. **a,** cells fed 100 μM N_3-Cho. **b**, cells feld 50 μM Inos-N_3. **c**, cells fed 250 μM C-L-Ser-N_3. **d**, cells fed 50 μM Ac_4ManNAz. LSM images were used for quantification. *n* = 25 cells per condition.

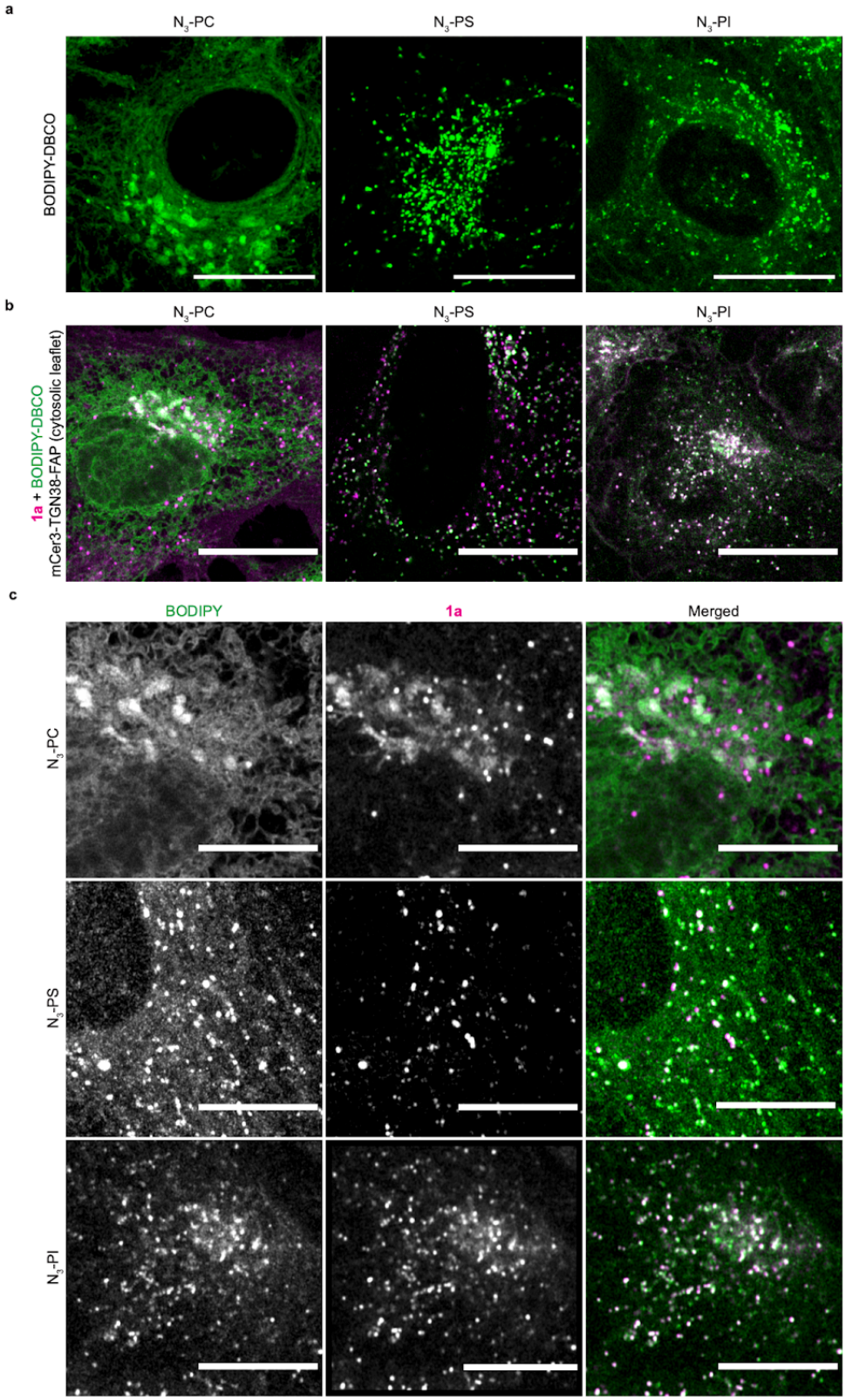
a
N3-PC
N3-PS
N3-PI
BODIPY-DBCO
b
N3-PC
N3-PS
N3-PI
1a + BODIPY-DBCO
mCer3-TGN38-FAP (cytosolic leaflet)
c
BODIPY
1a
Merged
N3-PC
N3-PS
N3-PI

684 **Supplementary Fig. 9. Multicolor imaging of global and targeted phospholipid pools**
685 Cells were metabolically labeled with 100 μM N_3-Cho, 250 μM C-L-Ser-N_3, or 50 μM Inos-N_3 for
686 24h prior to SPAAC conjugation. **a**, HeLa cells stained with 2 μM BODIPY-DBCO, which reacts
687 with intracellular azido lipids. Images reflect maximal projection of Airyscan z-stacked images.
688 Scale bars, 20 μm. **b**, Merged Airyscan images of HeLa cells stably expressing
689 pTet:mCer3-TGN38-FAP double stained with equimolar (1 μM each) **1a**:BODIPY-DBCO. Scale
690 bars, 20 μm **c**, Higher magnification images show overlapping phospholipid distributions
691 between total lipids labeled with BODIPY and those labeled by **1a** and detected in the cytosolic
692 leaflet of the TGN. For experiments **b-c**, 488 and 633 nm laser lines were used for imaging to
693 avoid excitation of mCer3. Scale = 10 μm.
694

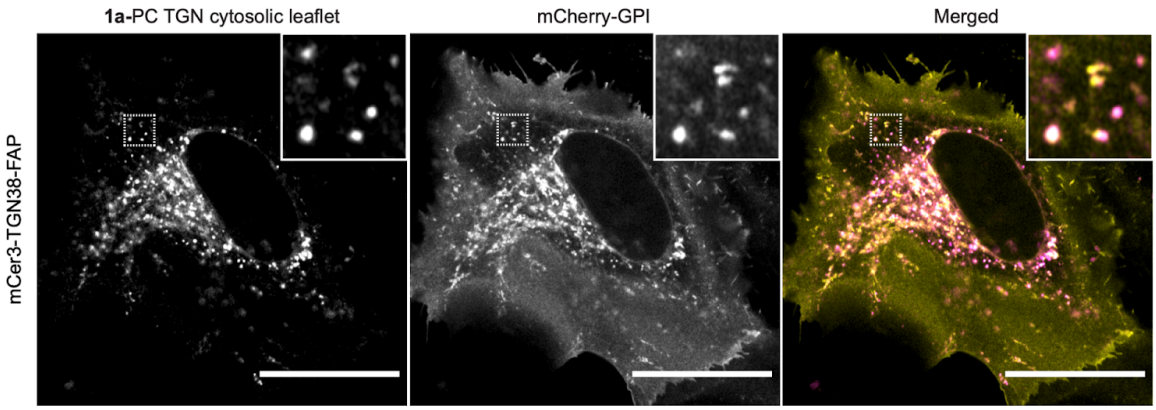

Supplementary Fig. 10. GPI-anchored proteins co-localize with cytoplasmic 1a-PC in TGN vesicles

Cells were cotransfected with mCherry-GPI and mCer3-TGN38-FAP constructs, fed 100 μM N_3-Cho for 24h, and labeled with 500 nM **1a.** Airyscan images were acquired using only 561 and 633 lasers for excitation of m-Cherry-GPI and **1a**-PC, respectively. Maximal projection of z-stacked images show co-localization between mCherry-GPI cargo and cytosolic facing **1a**-PC in TGN cisternae and vesicles (inset). Scale = 25 μm.

706

707

708 **Supplementary Movie 1: Mobility of TGN vesicles containing cytosolic PC and luminal SM**

709 Airyscan time-lapse of Golgi from the cell shown in Fig. 4d expressing GFP-EqtSM (cyan) and
710 mCer3-TGN38-FAP detecting **1a**-PC detection in the cytoplasmic leaflet (magenta). Images
711 reflect maximal intensity values from z-stacked images spanning 1.5 µm. Scale = 10 µm.

712 https://drive.google.com/file/d/1uWdM-LxW6N6hfmS_1oAvt9gelVmVm2tq/view?usp=sharing

713

714 **Supplementary Movie 2: Mobility of TGN vesicles containing cytosolic PC and protein**
715 **cargoes**

716 Airyscan time-lapse of Golgi from the cell shown in Supplementary Fig. 9 expressing
717 mCherry-SBP-GPI (yellow) and mCer3-TGN38-FAP detecting **1a**-PC detection in the
718 cytoplasmic leaflet (magenta). Scale = 20 µm.

719 https://drive.google.com/file/d/1S8RHj0p4P12DSThlM9wqXF7-yQTGs2qc/view?usp=sharing

720

721 **Supplementary Text: Synthesis of the Malachite Green Probes**

722

723 Commercially available 4-nitrobenzaldehyde, *N*,*N*-dimethylaniline, niobium(V) chloride ($NbCl_5$),
724 10% Pd/C, O-(7-azabenzotriazol-1-yl)- 1,1,3,3-tetramethyluronium hexafluoro-phosphate
725 (HATU), *N*,*N*-diisopropylethylamine (DIEA), tetrachloro-*p*-benzoquinone, and glacial acetic acid
726 (AcOH) were obtained from Sigma-Aldrich. DBCO-C_6-CO_2H, azido-PEG_2-CH_2CO_2H, and
727 DBCO-PEG_2-CO_2H were obtained from BroadPharm. Deuterated chloroform ($CDCl_3$) was
728 obtained from Cambridge Isotope Laboratories. All reagents obtained from commercial
729 suppliers were used without further purification unless otherwise noted. Analytical thin-layer
730 chromatography was performed on E. Merck silica gel 60 F_{254} plates. Silica gel flash
731 chromatography was performed using E. Merck silica gel (type 60SDS, 230-400 mesh). Solvent
732 mixtures for chromatography are reported as v/v ratios. HPLC analysis was carried out on an
733 Eclipse Plus C8 analytical column with *Phase A*/*Phase B* gradients [*Phase A*: H_2O with 0.1%
734 formic acid; *Phase B*: MeOH with 0.1% formic acid]. HPLC purification was carried out on
735 Zorbax SB-C18 semipreparative column with *Phase A*/*Phase B* gradients [*Phase A*: H_2O with
736 0.1% formic acid; *Phase B*: MeOH with 0.1% formic acid]. Proton nuclear magnetic resonance
737 (^{1}H NMR) spectra were recorded on a Jeol ECZL 400 MHz spectrometer, and were referenced
738 relative to residual proton resonances in $CDCl_3$ (at d 7.26 ppm) or CD_3OD (at d 4.87 or 3.31
739 ppm). ^{1}H NMR splitting patterns are assigned as singlet (s), doublet (d), triplet (t), quartet (q) or
740 pentuplet (p). All first-order splitting patterns were designated on the basis of the appearance of
741 the multiplet. Splitting patterns that could not be readily interpreted are designated as multiplet
742 (m) or broad (br). Carbon nuclear magnetic resonance (^{13}C NMR) spectra were recorded on a
743 Jeol ECZL 400 MHz spectrometer, and were referenced relative to residual proton resonances
744 in $CDCl_3$ (at d 77.16 ppm) or CD_3OD (at d 49.15 ppm). Electrospray Ionization-Time of Flight
745 (ESI-TOF) spectra were obtained on an Agilent 6230 TOF-MS.

746

747 4,4'-((4-nitrophenyl)methylene)bis(*N*,*N*-dimethylaniline) [O_2N-Malachite Green *(Leuco form)*][62,63]**.**
748 A mixture of 4-nitrobenzaldehyde (0.755 g, 5.0 mmol), *N*,*N*-dimethylaniline (1.90 mL, 15.0
749 mmol), and $NbCl_5$ (0.135 g, 0.5 mmol) was heated at 130 ºC for 2 h under Ar. Several color
750 changes were observed, from yellow to orange, and finally purple. Afterwards, the reaction
751 mixture was cooled to room temperature and diluted in EtOAc (20 mL) and H_2O (20 mL). The
752 aqueous layer was then extracted with EtOAc (3 × 10 mL), and the combined organic layers
753 were dried over anhydrous $MgSO_4$ and concentrated *in vacuo*. The crude was absorbed over
754 SiO_2, and then purified by flash column chromatography (10-20% EtOAc in hexanes), affording
755 1.486 g of O_2N-Malachite Green *(Leuco form)* as an orange solid [79%, Rf = 0.42 (20% EtOAc
756 in hexanes)]. ^{1}H NMR ($CDCl_3$, 400.13 MHz, d): 8.12 (d, *J* = 8.7 Hz, 2H, 2 × CH), 7.30 (d, *J* = 8.7
757 Hz, 2H, 2 × CH), 6.96 (d, *J* = 8.7 Hz, 4H, 4 × CH), 6.69 (d, *J* = 8.2 Hz, 4H, 4 × CH), 5.47 (s, 1H,
758 1 × CH), 2.94 (s, 12H, 4 × CH_3). ^{13}C NMR ($CDCl_3$, 100.61 MHz, d): 153.3, 149.2, 146.3, 131.1,
759 130.2, 130.0, 123.6, 112.8, 55.0, 40.8. MS (ESI-TOF) [m/z (%)]: 376 ($[MH]^+$, 34), 188 ($[MH]^{2+}$,
760 100).
761
762 4,4'-((4-aminophenyl)methylene)bis(*N*,*N*-dimethylaniline) [H_2N-Malachite Green *(Leuco form)*]. A
763 suspension of 4,4'-((4-nitrophenyl)methylene)bis(*N*,*N*-dimethylaniline) [O_2N-Malachite Green
764 (*Leuco form*)), 150.0 mg, 0.40 mmol] and 10% Pd/C (42.6 mg) in absolute EtOH (8 mL) was
765 stirred for 2 h under H_2. Then, the mixture was filtered through a pad of celite, washing with
766 EtOH (3 × 2 mL). Afterwards, the filtrate was concentrated *in vacuo*, affording 137.2 mg of
767 H_2N-Malachite Green (*Leuco form*) as a white solid [99%, Rf = 0.42 (20% EtOAc in hexanes)].
768 The product was used directly without any further purification. ^{1}H NMR ($CDCl_3$, 400.13 MHz, d):
769 7.00 (d, *J* = 8.7 Hz, 4H, 4 × CH), 6.92 (d, *J* = 8.3 Hz, 2H, 2 × CH), 6.69 (d, *J* = 8.7 Hz, 4H, 4 ×
770 CH), 6.61 (d, *J* = 8.3 Hz, 2H, 2 × CH), 5.29 (s, 1H, 1 × CH), 3.86 (br s, 2H, 1 × NH_2), 2.92 (s,
771 12H, 4 × CH_3). ^{13}C NMR ($CDCl_3$, 100.61 MHz, d): 148.8, 144.2, 135.8, 133.8, 130.2, 130.0,
772 115.2, 112.8, 54.2, 41.0. MS (ESI-TOF) [m/z (%)]: 346 ($[MH]^+$, 11), 173 ($[MH]^{2+}$, 100).

773

774 DBCO-C_6-Malachite Green (*Leuco form*). A solution of DBCO-C_6-CO_2H (19.3 µL, 57.9 mmol) in
775 100 µL of CH_2Cl_2 was stirred at 0 ºC for 10 min, and then HATU (24.2 mg, 63.7 mmol) and DIEA
776 (40.4 µL, 231.6 µmol) were successively added. After 10 min stirring at 0 ºC, a H_2N-Malachite
777 Green *(Leuco form)* (20.0 mg, 57.9 mmol) solution in 100 µL of CH_2Cl_2 containing DIEA (20.2
778 µL, 115.8 µmol) was added. After 1 h stirring at rt, the solvent was removed under reduced
779 pressure to give a blue oil. The corresponding residue was dissolved in MeOH (400 µL), filtered
780 using a 0.2 µm syringe-driven filter, and the crude solution was purified by HPLC, affording 29.2
781 mg of DBCO-C_6-Malachite Green *(Leuco form)* as a blue oil [72%, t_R = 10.8 min (Zorbax
782 SB-C18 semipreparative column, 50% *Phase A* in *Phase B*, 1 min, then 50-5% *Phase A* in
783 *Phase B*, 5 min, and then 5% *Phase A* in *Phase B*, 10 min)]. ^{1}H NMR ($CDCl_3$, 400.13 MHz, d):
784 7.78 (s, 1H, 1 × NH), 7.72-7.64 (m, 1H, 1 × CH), 7.50-7.28 (m, 7H, 7 × CH), 7.25-7.18 (m, 4H, 4
785 × CH), 7.08-6.94 (m, 6H, 6 × CH), 6.93-6.72 (m, 2H, 2 × CH), 5.38 (s, 1H, 1 × CH), 5.17 (d, J =
786 13.8 Hz, 1H, 0.5 × CH_2), 3.69 (d, J = 13.8 Hz, 1H, 0.5 × CH_2), 2.96 (s, 12H, 4 × CH_3), 2.29 (dt, J_1
787 = 16.0 Hz, J_2 = 6.0 Hz, 1H, 0.5 × CH_2), 2.10 (dt, J_1 = 17.1 Hz, J_2 = 6.8 Hz, 1H, 0.5 × CH_2),
788 2.02-1.81 (m, 2H, 1 × CH_2), 1.62-1.40 (m, 3H, 1.5 × CH_2), 1.39-1.21 (m, 1H, 0.5 × CH_2). ^{13}C
789 NMR ($CDCl_3$, 100.61 MHz, d): 173.8, 171.2, 151.7, 148.0, 132.5, 130.3, 129.8, 129.1, 128.6,
790 128.5, 128.4, 128.0, 127.3, 125.6, 123.1, 122.6, 119.9, 115.1, 108.0, 55.6, 54.7, 44.0, 36.8,
791 34.6, 25.1, 24.0. MS (ESI-TOF) [m/z (%)]: 661 ($[MHI]^+$, 5), 331 ($[MH]^{2+}$, 100).

792

793 DBCO-C_6-Malachite Green *(Chromatic form)* (**1a**). To a blue solution of DBCO-C_6-Malachite
794 Green *(Leuco form)* (4.0 mg, 6.1 µmol) and tetrachloro-*p*-benzoquinone (1.8 mg, 7.3 µmol) in
795 $CHCl_3$ (226 µL), glacial acetic acid (4.5 µL, 0.45 µmol) was added. The solution was stirred at
796 35 ºC for 2 h. Afterwards, the volatiles were removed under reduced pressure, obtaining a dark
797 green residue. The crude was absorbed over SiO_2, and then purified by flash column
798 chromatography (0-7% MeOH in CH_2Cl_2), affording 3.8 mg of DBCO-C_6-Malachite Green

(Chromatic form) as a dark green solid [90%, Rf = 0.57 (10% MeOH in CH_2Cl_2)]. ^{1}H NMR (CD_3OD, 400.13 MHz, d): 7.91-7.76 (m, 4H, 4 × CH), 7.71-7.64 (m, 1H, 1 × NH), 7.57-7.47 (m, 2H, 2 × CH), 7.44 (d, *J* = 9.0 Hz, 4H, 4 × CH), 7.37 (d, *J* = 8.7 Hz, 2H, 2 × CH), 7.33-7.19 (m, 4H, 4 × CH), 7.06 (d, *J* = 9.4 Hz, 4H, 4 × CH), 4.93-4.91 (m, 2H, 1 × CH_2), 3.33 (s, 12H, 4 × CH_3), 2.52-2.45 (m, 2H, 1 × CH_2), 2.44-2.34 (m, 2H, 1 × CH_2), 1.83-1.65 (m, 4H, 2 × CH_2). ^{13}C NMR (CD_3OD, 100.61 MHz, d): 178.9, 174.7, 158.4, 145.6, 141.9, 137.7, 135.8, 135.6, 134.2, 133.5, 130.8, 130.4, 130.0, 129.7, 129.2, 128.9, 128.8, 128.3, 126.5, 125.6, 124.3, 123.1, 120.7, 120.2, 114.8, 114.5, 114.2, 40.9, 37.7, 34.4, 33.1, 30.8, 26.0, 25.5. MS (ESI-TOF) [m/z (%)]: 660 ($[MH -Cl]^+$, 51), 659 ($[M -Cl]^+$, 100), 330 ($[MH -Cl]^{2+}$, 53).

<u>DBCO-PEG$_2$-Malachite Green *(Leuco form)*.</u> A solution of DBCO-PEG$_2$-CO_2H (13.4 mg, 28.9 mmol) in 200 µL of CH_2Cl_2/DMF (1:1) was stirred at 0 ºC for 10 min, and then HATU (12.1 mg, 31.8 mmol) and DIEA (20.2 µL, 115.8 µmol) were successively added. After 10 min stirring at 0 ºC, a H_2N-Malachite Green *(Leuco form)* (10.0 mg, 28.9 mmol) solution in 200 µL of CH_2Cl_2/DMF (1:1) containing DIEA (10.1 µL, 57.9 µmol) was added. After 1 h stirring at rt, the solvent was removed under reduced pressure to give a blue oil. The corresponding residue was dissolved in MeOH (200 µL), filtered using a 0.2 µm syringe-driven filter, and the crude solution was purified by HPLC, affording 13.2 mg of DBCO-PEG$_2$-Malachite Green *(Leuco form)* as a blue oil [55%, t_R = 50.9 min (Zorbax SB-C18 semipreparative column, 95% *Phase A* in *Phase B*, 1 min, then 95-50% *Phase A* in *Phase B*, 30 min, and then 50-0% *Phase A* in *Phase B*, 22 min)]. ^{1}H NMR ($CDCl_3$, 400.13 MHz, d): 8.76 (s, 1H, 1 × NH), 7.60-7.54 (m, 1H, 1 × CH), 7.53-7.46 (m, 1H, 1 × CH), 7.46-7.34 (m, 6H, 6 × CH), 7.25-7.17 (m, 4H, 4 × CH), 7.09-6.96 (m, 6H, 6 × CH), 6.95-6.72 (m, 2H, 2 × CH), 6.28 (t, *J* = 5.6 Hz, 1H, 1 × NH), 5.36 (s, 1H, 1 × CH), 5.09 (d, *J* = 13.9 Hz, 1H, 0.5 × CH_2), 3.87-3.71 (m, 2H, 1 × CH_2), 3.69-3.56 (m, 5H, 2.5 × CH_2), 3.45 (t, *J* = 5.4 Hz, 2H, 1 × CH_2), 3.34-3.18 (m, 2H, 1 × CH_2), 2.95 (s, 12H, 4 × CH_3), 2.87-2.75 (m, 1H, 0.5 × CH_2), 2.53-2.41 (m, 2H, 1 × CH_2), 2.39-2.26 (m, 1H, 0.5 × CH_2), 2.17-2.02 (m, 1H,

825 0.5 × CH_2), 1.98-1.83 (m, 1H, 0.5 × CH_2). ^{13}C NMR ($CDCl_3$, 100.61 MHz, d): 172.7, 172.1,
826 169.9, 151.3, 148.1, 132.3, 130.3, 129.8, 129.5, 128.9, 128.4, 128.2, 127.9, 127.2, 125.6, 123.2,
827 122.6, 119.9, 114.8, 108.0, 70.7, 69.9, 69.8, 67.4, 55.8, 54.8, 39.1, 38.0, 31.5, 30.3. MS
828 (ESI-TOF) [m/z (%)]: 793 ($[MH]^+$, 4), 397 ($[MH]^{2+}$, 100).

829

830 DBCO-PEG$_2$-Malachite Green *(Chromatic form)* (**1b**). To a blue solution of
831 DBCO-PEG$_2$-Malachite Green *(Leuco form)* (5.0 mg, 6.3 μmol) and tetrachloro-*p*-benzoquinone
832 (1.9 mg, 7.6 μmol) in $CHCl_3$ (235 μL), glacial acetic acid (4.7 μL, 0.47 μmol) was added. The
833 solution was stirred at 35 ºC for 2 h. Afterwards, the volatiles were removed under reduced
834 pressure, obtaining a dark green residue. The crude was absorbed over SiO_2, and then purified
835 by flash column chromatography (0-10% MeOH in CH_2Cl_2), affording 4.8 mg of
836 N_3-PEG$_2$-Malachite Green *(Chromatic form)* as a dark green solid [92%, Rf = 0.44 (10% MeOH
837 in CH_2Cl_2)]. ^1H NMR ($CDCl_3$, 400.13 MHz, d): 11.33 (s, 1H, 1 × NH), 8.20 (d, *J* = 8.4 Hz, 2H, 2 ×
838 CH), 7.85-7.69 (m, 1H, 1 × NH), 7.63 (d, *J* = 7.3 Hz, 1H, 1 × CH), 7.58 (d, *J* = 7.6 Hz, 1H, 1 ×
839 CH), 7.42-7.27 (m, 9H, 9 × CH), 7.25-7.17 (m, 3H, 3 × CH), 6.86 (d, *J* = 8.5 Hz, 4H, 4 × CH),
840 5.13 (d, *J* = 13.9 Hz, 1H, 0.5 × CH_2), 3.91 (t, *J* = 5.9 Hz, 2H, 1 × CH_2), 3.76-3.57 (m, 5H, 2.5 ×
841 CH_2), 3.56-3.45 (m, 2H, 1 × CH_2), 3.31 (s, 12H, 4 × CH_3), 2.94 (t, *J* = 5.9 Hz, 2H, 1 × CH_2),
842 2.87-2.75 (m, 1H, 0.5 × CH_2), 2.68-2.53 (m, 1H, 0.5 × CH_2), 2.46-2.26 (m, 4H, 2 × CH_2). ^{13}C
843 NMR ($CDCl_3$, 100.61 MHz, d): 175.7, 174.4, 172.4, 156.5, 146.3, 141.1, 137.4, 134.2, 133.4,
844 133.3, 132.3, 129.3, 127.7, 127.6, 125.8, 124.9, 124.4, 122-1, 121.9, 120.0, 119.9, 117.3, 113.6,
845 133.5, 98.1, 98.0, 70.4, 70.3, 68.9, 67.3, 47.0, 41.2, 40.4, 38.0, 32.1, 29.9, 29.5, 22.9*, 14.3*.
846 MS (ESI-TOF) [m/z (%)]: 791 ($[MH -Cl]^+$, 3), 396 ($[MH -Cl]^{2+}$, 100). *Artifact.

847

848

^{1}H (left) and ^{13}C NMR (right) spectra of synthesized compounds and key intermediates

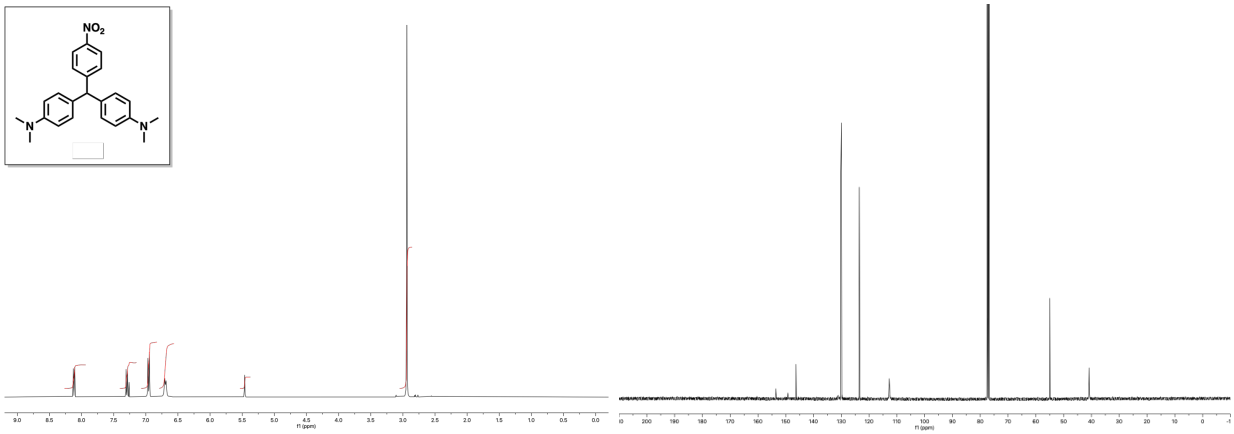

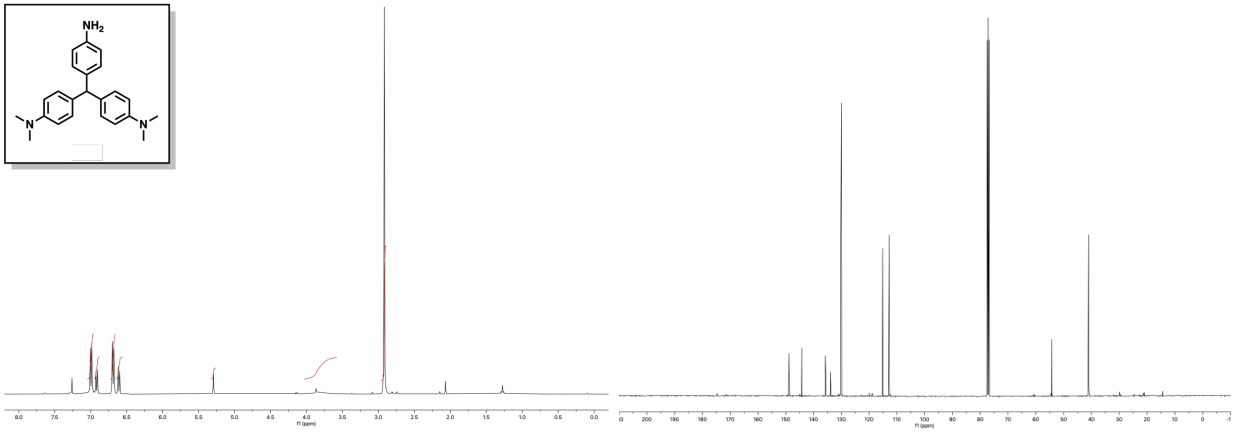

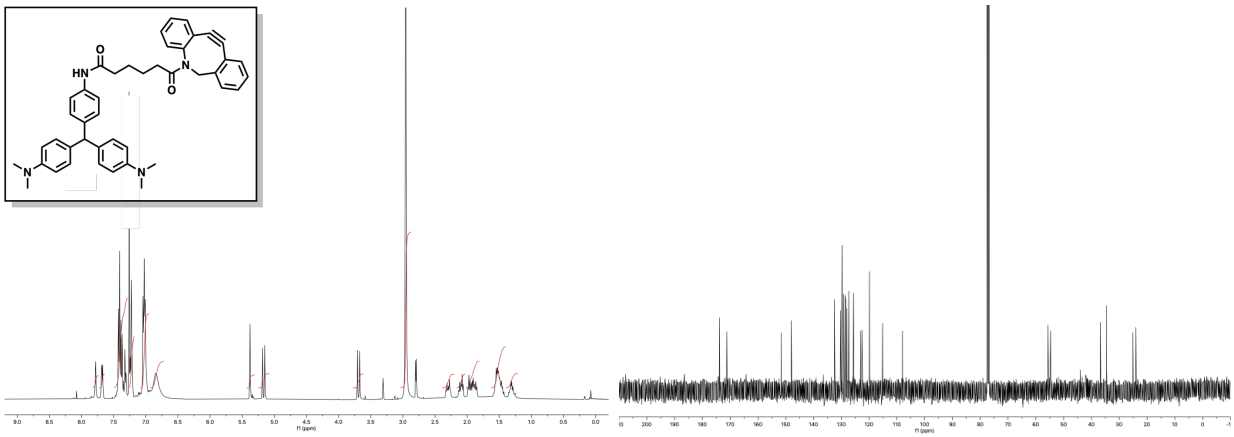

853

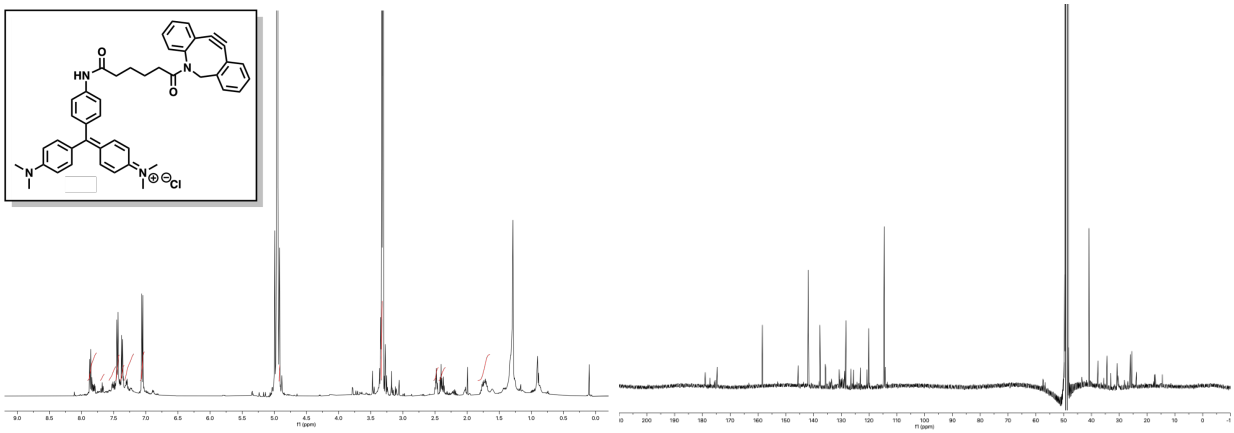

854

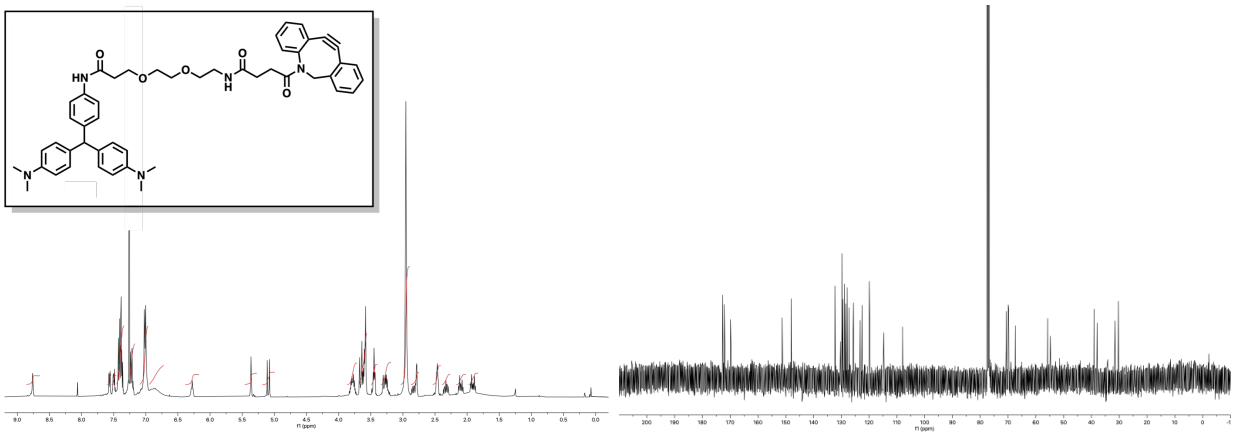

855

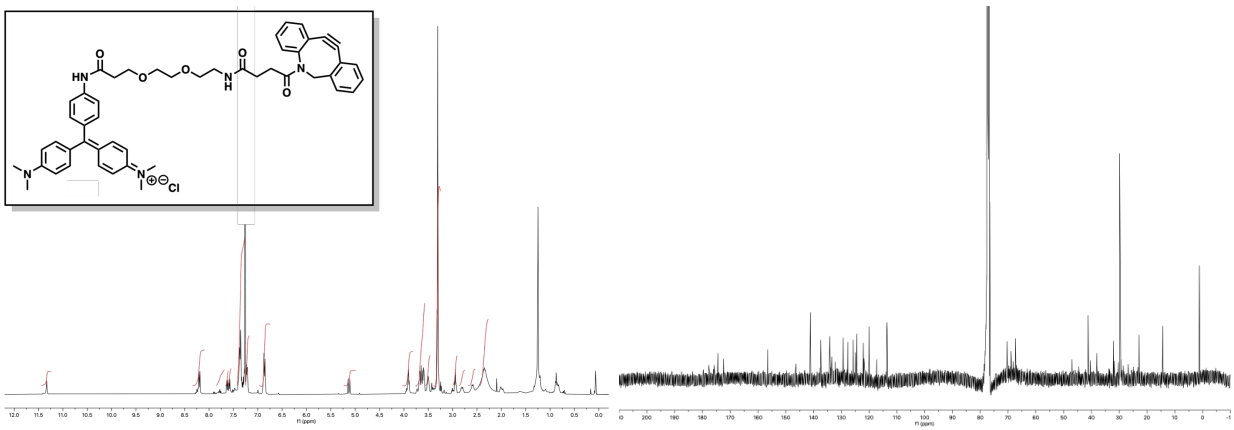

856

References

1. van Meer, G., Voelker, D. R. & Feigenson, G. W. Membrane lipids: where they are and how they behave. *Nat. Rev. Mol. Cell Biol.* **9**, 112–124 (2008).
2. Levental, I. & Lyman, E. Regulation of membrane protein structure and function by their lipid nano-environment. *Nat. Rev. Mol. Cell Biol.* **24**, 107–122 (2023).
3. Lorent, J. H. *et al.* Plasma membranes are asymmetric in lipid unsaturation, packing and protein shape. *Nat. Chem. Biol.* **16**, 644–652 (2020).
4. Jao, C. Y., Roth, M., Welti, R. & Salic, A. Metabolic labeling and direct imaging of choline phospholipids in vivo. *Proc. Natl. Acad. Sci. U. S. A.* **106**, 15332–15337 (2009).
5. Ancajas, C. F. *et al.* Cellular labeling of phosphatidylserine using clickable Serine probes. *ACS Chem. Biol.* **18**, 377–384 (2023).
6. Ricks, T. J. *et al.* Labeling of Phosphatidylinositol Lipid Products in Cells through Metabolic Engineering by Using a Clickable myo-Inositol Probe. *Chembiochem* **20**, 172–180 (2019).
7. Bumpus, T. W. & Baskin, J. M. A Chemoenzymatic Strategy for Imaging Cellular Phosphatidic Acid Synthesis. *Angew. Chem. Int. Ed Engl.* **55**, 13155–13158 (2016).
8. Bussink, A. P. *et al.* N-azidoacetylmannosamine-mediated chemical tagging of gangliosides. *J. Lipid Res.* **48**, 1417–1421 (2007).
9. Tamura, T. *et al.* Organelle membrane-specific chemical labeling and dynamic imaging in living cells. *Nat. Chem. Biol.* **16**, 1361–1367 (2020).
10. Maekawa, M., Yang, Y. & Fairn, G. D. Perfringolysin O Theta Toxin as a Tool to Monitor the Distribution and Inhomogeneity of Cholesterol in Cellular Membranes. *Toxins* **8**, (2016).
11. Deng, Y., Rivera-Molina, F. E., Toomre, D. K. & Burd, C. G. Sphingomyelin is sorted at the trans Golgi network into a distinct class of secretory vesicle. *Proc. Natl. Acad. Sci. U. S. A.* **113**, 6677–6682 (2016).
12. Gallo, E. Fluorogen-Activating Proteins: Next-Generation Fluorescence Probes for

883 Biological Research. *Bioconjug. Chem.* **31**, 16–27 (2020).

884 13. Kozma, E. & Kele, P. Fluorogenic probes for super-resolution microscopy. *Org. Biomol.*
885 *Chem.* **17**, 215–233 (2019).

886 14. Bottone, S. *et al.* A fluorogenic chemically induced dimerization technology for controlling,
887 imaging and sensing protein proximity. *Nat. Methods* **20**, 1553–1562 (2023).

888 15. Yan, Q. *et al.* Localization microscopy using noncovalent fluorogen activation by genetically
889 encoded fluorogen-activating proteins. *Chemphyschem* **15**, 687–695 (2014).

890 16. Horibata, Y. & Sugimoto, H. Differential contributions of choline phosphotransferases CPT1
891 and CEPT1 to the biosynthesis of choline phospholipids. *J. Lipid Res.* **62**, 100100 (2021).

892 17. Ng, M. N. P., Kitos, T. E. & Cornell, R. B. Contribution of lipid second messengers to the
893 regulation of phosphatidylcholine synthesis during cell cycle re-entry. *Biochim. Biophys.*
894 *Acta* **1686**, 85–99 (2004).

895 18. Adibhatla, R. M., Hatcher, J. F. & Gusain, A. Tricyclodecan-9-yl-xanthogenate (D609)
896 mechanism of actions: a mini-review of literature. *Neurochem. Res.* **37**, 671–679 (2012).

897 19. Larsen, E. C., Hatcher, J. F. & Adibhatla, R. M. Effect of tricyclodecan-9-yl potassium
898 xanthate (D609) on phospholipid metabolism and cell death during oxygen-glucose
899 deprivation in PC12 cells. *Neuroscience* **146**, 946–961 (2007).

900 20. Stephan, T., Roesch, A., Riedel, D. & Jakobs, S. Live-cell STED nanoscopy of
901 mitochondrial cristae. *Sci. Rep.* **9**, 12419 (2019).

902 21. John Peter, A. T., Petrungaro, C., Peter, M. & Kornmann, B. METALIC reveals
903 interorganelle lipid flux in live cells by enzymatic mass tagging. *Nat. Cell Biol.* **24**, 996–1004
904 (2022).

905 22. Kumar, N. *et al.* VPS13A and VPS13C are lipid transport proteins differentially localized at
906 ER contact sites. *J. Cell Biol.* **217**, 3625–3639 (2018).

907 23. Horibata, Y. *et al.* StarD7 Protein Deficiency Adversely Affects the Phosphatidylcholine
908 Composition, Respiratory Activity, and Cristae Structure of Mitochondria. *J. Biol. Chem.*

291, 24880–24891 (2016).

24. Horibata, Y. & Sugimoto, H. StarD7 mediates the intracellular trafficking of phosphatidylcholine to mitochondria. *J. Biol. Chem.* **285**, 7358–7365 (2010).

25. Horibata, Y. *et al.* Identification of the N-terminal transmembrane domain of StarD7 and its importance for mitochondrial outer membrane localization and phosphatidylcholine transfer. *Sci. Rep.* **7**, 8793 (2017).

26. Rothman, J. E. & Lenard, J. Membrane asymmetry. *Science* **195**, 743–753 (1977).

27. Verkleij, A. J. *et al.* The asymmetric distribution of phospholipids in the human red cell membrane. A combined study using phospholipases and freeze-etch electron microscopy. *Biochim. Biophys. Acta* **323**, 178–193 (1973).

28. Bos, K., Wraight, C. & Stanley, K. K. TGN38 is maintained in the trans-Golgi network by a tyrosine-containing motif in the cytoplasmic domain. *EMBO J.* **12**, 2219–2228 (1993).

29. Luzio, J. P. *et al.* Identification, sequencing and expression of an integral membrane protein of the trans-Golgi network (TGN38). *Biochem. J* **270**, 97–102 (1990).

30. Iyoshi, S. *et al.* Asymmetrical distribution of choline phospholipids revealed by click chemistry and freeze-fracture electron microscopy. *ACS Chem. Biol.* **9**, 2217–2222 (2014).

31. Cabukusta, B. *et al.* A lipid transfer protein knockout library reveals ORP9-ORP11 dimer mediating PS/PI(4)P exchange at the ER-trans Golgi contact site to promote sphingomyelin synthesis. *bioRxiv* 2023.06.02.543249 (2023) doi:10.1101/2023.06.02.543249.

32. Phillips, S. E., Ile, K. E., Boukhelifa, M., Huijbregts, R. P. H. & Bankaitis, V. A. Specific and nonspecific membrane-binding determinants cooperate in targeting phosphatidylinositol transfer protein beta-isoform to the mammalian trans-Golgi network. *Mol. Biol. Cell* **17**, 2498–2512 (2006).

33. Fairn, G. D. *et al.* High-resolution mapping reveals topologically distinct cellular pools of phosphatidylserine. *J. Cell Biol.* **194**, 257–275 (2011).

34. Saxon, E. & Bertozzi, C. R. Cell surface engineering by a modified Staudinger reaction.

935 *Science* **287**, 2007–2010 (2000).

936 35. Fleischer, B. Mechanism of glycosylation in the Golgi apparatus. *J. Histochem. Cytochem.*
937 **31**, 1033–1040 (1983).

938 36. Klemm, R. W. *et al.* Segregation of sphingolipids and sterols during formation of secretory
939 vesicles at the trans-Golgi network. *J. Cell Biol.* **185**, 601–612 (2009).

940 37. Doktorova, M. *et al.* Cell Membranes Sustain Phospholipid Imbalance Via Cholesterol
941 Asymmetry. *bioRxiv* 2023.07.30.551157 (2023) doi:10.1101/2023.07.30.551157.

942 38. Boyce, M. *et al.* Metabolic cross-talk allows labeling of O-linked
943 β-*N*-acetylglucosamine-modified proteins via the *N*-acetylgalactosamine salvage pathway.
944 *Proceedings of the National Academy of Sciences* **108**, 3141–3146 (2011).

945 39. Hang, H. C., Yu, C., Kato, D. L. & Bertozzi, C. R. A metabolic labeling approach toward
946 proteomic analysis of mucin-type O-linked glycosylation. *Proc. Natl. Acad. Sci. U. S. A.* **100**,
947 14846–14851 (2003).

948 40. Ma, Z. & Vosseller, K. Cancer Metabolism and Elevated O-GlcNAc in Oncogenic Signaling*.
949 *J. Biol. Chem.* **289**, 34457–34465 (2014).

950 41. Tan, E. P. *et al.* Sustained O-GlcNAcylation reprograms mitochondrial function to regulate
951 energy metabolism. *J. Biol. Chem.* **292**, 14940–14962 (2017).

952 42. Zhu, Q. *et al.* *O*-GlcNAcylation promotes tumor immune evasion by inhibiting PD-L1
953 lysosomal degradation. *Proceedings of the National Academy of Sciences* **120**,
954 e2216796120 (2023).

955 43. Pekkurnaz, G., Trinidad, J. C., Wang, X., Kong, D. & Schwarz, T. L. Glucose regulates
956 mitochondrial motility via Milton modification by O-GlcNAc transferase. *Cell* **158**, 54–68
957 (2014).

958 44. Dupas, T. *et al.* An overview of tools to decipher O-GlcNAcylation from historical
959 approaches to new insights. *Int. J. Biochem. Cell Biol.* **151**, 106289 (2022).

960 45. Onodera, Y., Nam, J.-M. & Bissell, M. J. Increased sugar uptake promotes oncogenesis via

961 EPAC/RAP1 and O-GlcNAc pathways. *J. Clin. Invest.* **124**, 367–384 (2014).

962 46. Jóźwiak, P. *et al.* Mitochondrial O-GlcNAc Transferase Interacts with and Modifies Many
963 Proteins and Its Up-Regulation Affects Mitochondrial Function and Cellular Energy
964 Homeostasis. *Cancers* **13**, (2021).

965 47. Ma, J. *et al.* O-GlcNAcomic Profiling Identifies Widespread O-Linked
966 β-N-Acetylglucosamine Modification (O-GlcNAcylation) in Oxidative Phosphorylation
967 System Regulating Cardiac Mitochondrial Function. *J. Biol. Chem.* **290**, 29141–29153
968 (2015).

969 48. Guzmán, L. E. *et al.* Bioorthogonal Metabolic Labeling of the Virulence Factor Phenolic
970 Glycolipid in Mycobacteria. *ACS Chem. Biol.* (2024) doi:10.1021/acschembio.3c00724.

971 49. Fantoni, N. Z., El-Sagheer, A. H. & Brown, T. A Hitchhiker's Guide to Click-Chemistry with
972 Nucleic Acids. *Chem. Rev.* **121**, 7122–7154 (2021).

973 50. Liang, D. *et al.* A real-time, click chemistry imaging approach reveals stimulus-specific
974 subcellular locations of phospholipase D activity. *Proc. Natl. Acad. Sci. U. S. A.* **116**,
975 15453–15462 (2019).

976 51. Nguyen, S. S. & Prescher, J. A. Developing bioorthogonal probes to span a spectrum of
977 reactivities. *Nat Rev Chem* **4**, 476–489 (2020).

978 52. Gautier, A. Fluorescence-Activating and Absorption-Shifting Tags for Advanced Imaging
979 and Biosensing. *Acc. Chem. Res.* **55**, 3125–3135 (2022).

980 53. Muslinkina, L. *et al.* Structure-Based Rational Design of Two Enhanced Bacterial Lipocalin
981 Blc Tags for Protein-PAINT Super-resolution Microscopy. *ACS Chem. Biol.* **15**, 2456–2465
982 (2020).

983 54. Wong, L. H., Gatta, A. T. & Levine, T. P. Lipid transfer proteins: the lipid commute via
984 shuttles, bridges and tubes. *Nat. Rev. Mol. Cell Biol.* **20**, 85–101 (2019).

985 55. Sakuragi, T. & Nagata, S. Regulation of phospholipid distribution in the lipid bilayer by
986 flippases and scramblases. *Nat. Rev. Mol. Cell Biol.* **24**, 576–596 (2023).

987 56. Surma, M. A., Klose, C. & Simons, K. Lipid-dependent protein sorting at the trans-Golgi
988 network. *Biochim. Biophys. Acta* **1821**, 1059–1067 (2012).
989 57. Sebastian, T. T., Baldridge, R. D., Xu, P. & Graham, T. R. Phospholipid flippases: building
990 asymmetric membranes and transport vesicles. *Biochim. Biophys. Acta* **1821**, 1068–1077
991 (2012).
992 58. Sharpe, H. J., Stevens, T. J. & Munro, S. A comprehensive comparison of transmembrane
993 domains reveals organelle-specific properties. *Cell* **142**, 158–169 (2010).
994 59. Carpenter, M. A. *et al.* Protein Proximity Observed Using Fluorogen Activating Protein and
995 Dye Activated by Proximal Anchoring (FAP-DAPA) System. *ACS Chem. Biol.* **15**,
996 2433–2443 (2020).
997 60. Telmer, C. A. *et al.* Rapid, specific, no-wash, far-red fluorogen activation in subcellular
998 compartments by targeted fluorogen activating proteins. *ACS Chem. Biol.* **10**, 1239–1246
999 (2015).
1000 61. Kowarz, E., Löscher, D. & Marschalek, R. Optimized Sleeping Beauty transposons rapidly
1001 generate stable transgenic cell lines. *Biotechnol. J.* **10**, 647–653 (2015).
1002 62. Montagut, A. M., Gálvez, E., Shafir, A., Sebastián, R. M. & Vallribera, A. Triarylmethane
1003 Dyes for Artificial Repellent Cotton Fibers. *Chemistry* **23**, 3810–3814 (2017).
1004 63. Kim, J., Park, E. Y., Moon, S.-Y., Kim, J.-M. & Park, K. Patterned color images with a
1005 triphenylmethane-derived acrylate polymer. *Macromol. Res.* **16**, 81–83 (2008).

1006